

Staircase solutions and stability in vertically confined salt-finger convection

Chang Liu^{1†}, Keith Julien² and Edgar Knobloch¹

¹Department of Physics, University of California, Berkeley, CA 94720, USA

²Department of Applied Mathematics, University of Colorado, Boulder, CO 80309, USA

(Received xx; revised xx; accepted xx)

Bifurcation analysis of confined salt-finger convection using single-mode equations obtained from a severely truncated Fourier expansion in the horizontal is performed. Strongly nonlinear staircase-like solutions having, respectively, one (S1), two (S2) and three (S3) regions of well-mixed salinity in the vertical direction are computed using numerical continuation, and their stability properties are determined. Near onset, the one-layer S1 solution is stable and corresponds to maximum salinity transport among the three solutions. The S2 and S3 solutions are unstable but exert an influence on the statistics observed in direct numerical simulations (DNS) in larger two-dimensional (2D) domains. Secondary bifurcations of S1 lead either to tilted-finger (TF1) or to traveling wave (TW1) solutions, both accompanied by the spontaneous generation of large-scale shear, a process favored for lower density ratios and Prandtl numbers (Pr). These states at low Pr are associated, respectively, with two-layer and three-layer staircase-like salinity profiles in the mean. States breaking reflection symmetry in the midplane are also computed. In 2D and for low Pr the DNS results favor direction-reversing tilted fingers (RTF) resembling the pulsating wave state observed in other systems. Two-layer and three-layer mean salinity profiles corresponding to RTF and TW1 are observed in 2D DNS averaged over time. The single-mode solutions close to the high wavenumber onset are in an excellent agreement with 2D DNS in small horizontal domains and compare well with 3D DNS.

Key words: Salt-finger convection, single-mode equations, double-diffusive convection

1. Introduction

Oceanographic measurements have widely reported staircase-like structures with regions of nearly constant density in the vertical direction separated by interfaces with a sharp density gradient (Tait & Howe 1968, 1971; Schmitt *et al.* 1987, 2005; Padman & Dillon 1989; Muench *et al.* 1990; Zodiatis & Gasparini 1996; Morell *et al.* 2006; Timmermans *et al.* 2008; Fer *et al.* 2010; Spear & Thomson 2012). Such structures are typical of tropical and subtropical regions where warm salty water often overlies cold fresh water and have been ascribed to the presence of salt-finger convection. Indeed, staircases have been observed in the western tropical Atlantic (Schmitt *et al.* 1987, 2005), Tyrrhenian Sea (Zodiatis & Gasparini 1996), and the Mediterranean outflow in the Northeast Atlantic (Tait & Howe 1968, 1971), where conditions for salt-finger convection prevail. These staircases are typically characterized by a large coherence length in the horizontal, much larger than the step height

† Email address for correspondence: chang_liu@berkeley.edu

in the vertical. For example, the Caribbean-Sheets and Layers Transect (C-SALT) field programs show that the well-mixed layers were 5–30 m thick and laterally coherent over scales of 200–400 km (Schmitt *et al.* 1987). The presence of staircases also enhances the tracer mixing rate. For example, the North Atlantic Tracer Release Experiments (NATRE) (Schmitt *et al.* 2005) reveal a mixing rate in the western tropical Atlantic five times larger than that in the eastern subtropical Atlantic. Spontaneous formation of staircases has also been observed in idealized laboratory experiments (Linden 1978; Krishnamurti 2003, 2009) and direct numerical simulations (DNS) (Piacsek & Toomre 1980; Radko 2003, 2005; Stellmach *et al.* 2011; Yang *et al.* 2020).

Understanding the origin of spontaneous staircase formation is important for parameterization and accurate modeling of oceanographic processes. Various mechanisms for staircase formation have been proposed (Radko 2013, §8). The collective instability mechanism (Stern 1969; Holyer 1981) identifies conditions for the formation of a staircase based on the instability of the salt-finger field to internal gravity waves, but requires a closure model for the Reynolds stress and the temperature and salinity fluxes based on laboratory measurement and ocean observation. The onset of staircase formation is also predicted by models with negative density diffusion (Phillips 1972; Posmentier 1977). The related γ -instability of Radko (2003) requires a parameterization of the Nusselt number and the flux ratio but shows good agreement with 2D and 3D direct numerical simulation of salt-finger convection (Radko 2003; Stellmach *et al.* 2011). However, these predictions generally only focus on the onset of a large-scale instability suggesting the appearance of a staircase, but do not provide a detailed profile of the final staircase or its parameter dependence. In this connection the model of Balmforth *et al.* (1998) is of particular interest. The model parametrizes the coupling between buoyancy flux and local turbulent kinetic energy but succeeds in generating robust staircases. Nevertheless, the use of closure models employed in all these predictions results in uncertainty in the applicable parameter regime.

This work aims to discuss an alternative mechanism for spontaneous staircase formation from a bifurcation theory point of view, focusing on the computation of strongly nonlinear staircase-like solutions and analyzing their stability. Bifurcation analysis has been widely employed to provide insight into pattern formation in fluid dynamics (Crawford & Knobloch 1991). For example, a secondary bifurcation of steady convection rolls in Rayleigh-Bénard convection to tilted rolls was shown to be accompanied by the generation of large-scale shear (Howard & Krishnamurti 1986; Rucklidge & Matthews 1996), resembling both experimental observation (Krishnamurti & Howard 1981) and direct numerical simulations (Goluskin *et al.* 2014). A sequence of local and global bifurcations of such tilted convection cells in magnetoconvection was shown to lead to a pulsating wave characterized by periodic reversals in the direction of the tilt and the accompanying large-scale shear (Matthews *et al.* 1993; Proctor & Weiss 1993; Proctor *et al.* 1994; Rucklidge & Matthews 1996). In the diffusive configuration in which cold fresh water overlies warm salty water, a similar analysis found stable traveling waves near onset (Knobloch *et al.* 1986) and provided insight into the transition to chaos (Knobloch *et al.* 1992). Such chaotic or even fully developed turbulent states generally visit neighborhoods of (unstable) steady, periodic, or traveling wave solutions, and these visits leave an imprint on the flow statistics; see, e.g., Kawahara & Kida (2001); van Veen *et al.* (2006) and the reviews by Kawahara *et al.* (2012); Graham & Floryan (2021).

This work focuses on vertically confined salt-finger convection in order to understand the interior between two well-mixed layers. While stress-free velocity boundary conditions are suitable for understanding oceanographic scenarios, no-slip boundary conditions are more relevant to laboratory experiments (Hage & Tilgner 2010). A wide range of bifurcation analyses of related problems have been performed on vertically confined systems with different boundary conditions including Rayleigh-Bénard convection. In the salt-finger case

the fluxes generated in a vertically confined system agree quantitatively with those obtained in a vertically periodic domain when normalized by the bulk conductive fluxes (Li & Yang 2022) despite the elimination of the elevator mode that is present in vertically periodic domains; see, e.g., Stern (1969); Holyer (1984); Radko (2013, §2.1).

In order to facilitate bifurcation analysis, we focus here on the single-mode equations obtained from a severely truncated Fourier expansion in the horizontal. Such single-mode equations reduce the two (or three) spatial dimensions in the primitive equations into one vertical dimension, with the dependence on the horizontal direction parameterized by a single assumed horizontal wavenumber. Such a truncation may provide insight into salt-finger convection as the underlying flow structures are dominated by well-organized columnar structures; see, e.g., the visualization of confined salt-finger convection by Yang *et al.* (2016a, figure 7). This single-mode formulation also explicitly isolates and describes the interaction between horizontally averaged modes (corresponding to the staircase or large-scale shear) and the horizontal harmonics (corresponding to fingers), in the spirit of mean-field theory; see, e.g., (Garaud 2018, §3.2.1). Moreover, the single-mode equations do not require any closure assumptions for the Reynolds stress and the temperature and salinity fluxes to parametrize the feedback between the fluctuations and horizontally averaged quantities, while preserving the nonlinear interaction between them; see figure 1(b) below.

Single-mode equations have been widely employed to provide insight into related problems. For example, single-mode solutions (also called ‘single- α mean-field theory’) for Rayleigh-Bénard convection with stress-free boundary conditions have been shown to reproduce the mean temperature profile expected at a high Rayleigh number (Herring 1963). For no-slip boundaries at high Prandtl numbers, the Nusselt number predicted from this framework is within 20% of the experimental value, and the root-mean-square velocity and temperature fluctuations also resemble the profiles seen in experimental measurements (Herring 1964). The single-mode theory has since been extended to the time-dependent problem (Elder 1969) and to more general planforms (e.g., hexagonal) (Gough *et al.* 1975; Toomre *et al.* 1977), showing qualitative agreement with experimental results. The vertical vorticity mode was included within the single-mode equations with hexagon planform by (Lopez & Murphy 1983; Murphy & Lopez 1984; Massaguer & Mercader 1988; Massaguer *et al.* 1990) and is excited beyond a secondary bifurcation of convection rolls. Such single-mode equations have also proved to provide insight into many other problems including rotating convection (Baker & Spiegel 1975), plane Poiseuille flow (Zahn *et al.* 1974) and double-diffusive convection (Gough & Toomre 1982; Paparella & Spiegel 1999; Paparella *et al.* 2002). In particular, DNS of single-mode solutions of salt-finger convection show that fingers can tilt leading to the spontaneous formation of large-scale shear, which may be steady or oscillate, together with a staircase-like profile in the horizontally averaged salinity (Paparella & Spiegel 1999; Paparella 1997). Moreover, in certain asymptotic regimes single-mode solutions may be exact; see, e.g., the high wavenumber (tall and thin) limit of Rayleigh-Bénard convection (Blennerhassett & Bassom 1994), convection in a porous medium (Lewis *et al.* 1997) or salt-finger convection (Proctor & Holyer 1986). Such high wavenumber regimes are naturally achieved in convection with strong restraints such as rapid rotation (Julien & Knobloch 1997) or strong magnetic field (Julien *et al.* 1999; Calkins *et al.* 2016; Plumley *et al.* 2018) and the resulting *exact* single-mode equations have proved immensely useful for understanding these systems; see the review by Julien & Knobloch (2007).

This work performs bifurcation analysis of vertically confined salt-finger convection using single-mode equations. The resulting equations are solved for the vertical structure of the solutions as a function of the density ratio, the Prandtl number and the assumed horizontal wavenumber. We fix the diffusivity ratio and thermal Rayleigh number and focus almost exclusively on no-slip velocity boundary conditions. We found staircase-like solutions with

one (S1), two (S2) and three (S3) well-mixed mean salinity steps in the vertical direction, all of which bifurcate from the trivial solution. In each case salinity gradients are expelled from regions of closed streamlines, leading to a well-mixed interior. Secondary bifurcations of S1 lead to either tilted fingers (TF1) or traveling waves (TW1), both of which break the horizontal reflection symmetry via the spontaneous formation of large-scale shear. Secondary bifurcations of S2 and S3 lead to asymmetric solutions (A2 and A3) that spontaneously break midplane reflection symmetry.

The stability and accuracy of the single-mode solutions are further analyzed with the assistance of 2D DNS. Near onset, the one-layer solution S1 is stable and corresponds to maximum salinity transport among all known solutions, a fact that is consistent with the prediction of the ‘relative stability’ criterion (Malkus & Veronis 1958). The associated Sherwood number (or salinity Nusselt number) near the high wavenumber onset is in excellent agreement with DNS in small horizontal domains. In large domains the DNS reveals a tendency to revert to the characteristic finger scale but the wavenumber of the final state exhibits strong dependence on initial condition (if the final state is steady) or the state may remain chaotic. The S2, S3, A2, and A3 solutions are all unstable within the explored parameter regimes, but may be imprinted on the statistics of the chaotic state. At lower density ratios, the S1, S2 and S3 salinity profiles all sharpen and the large-scale shear and tilt angle of the TF1 state increases. The TW1 solutions are also present in this regime, while low Prandtl numbers favor direction-reversing tilted fingers (RTF), a state in which the tilt direction and associated large-scale shear reverse periodically as in the pulsating wave.

The remainder of this paper is organized as follows. §2 describes the problem setup and the formulation of the single-mode equations. The equations are solved using numerical continuation and their stability properties are established for Prandtl number $Pr = 7$ in §3. The tilted finger and traveling wave states are analyzed for $Pr = 0.05$ in §4. The paper concludes with a brief summary and discussion in §5.

2. Single-mode equations for confined salt-finger convection

We consider a fluid between two infinitely long parallel plates separated by a distance h . The temperature and salinity at these two plates are maintained at constant values with the top plate maintained at a higher temperature and salinity, as illustrated in figure 1(a). The equation of state $(\rho_* - \rho_{r*})/\rho_{r*} = -\alpha(T_* - T_{r*}) + \beta(S_* - S_{r*})$ is linear, with constant expansion/contraction coefficients α , β and reference density, temperature, and salinity ρ_{r*} , T_{r*} , S_{r*} , respectively. The subscript $*$ denotes a dimensional variable. In the following we nondimensionalize the temperature T_* by the temperature difference between the top and bottom layer, $T = T_*/\Delta T$ ($\Delta T > 0$), and likewise for the salinity S_* , $S = S_*/\Delta S$ ($\Delta S > 0$). Spatial variables are nondimensionalized by the height h of the layer while time and velocity are nondimensionalized using the thermal diffusion time h^2/κ_T and the corresponding speed κ_T/h , respectively. Here κ_T is the thermal diffusivity. We decompose the temperature and salinity into a linear base state and deviation,

$$T = z + \tilde{T}, \quad S = z + \tilde{S}, \quad (2.1a-b)$$

and introduce the velocity field $\mathbf{u} := (u, v, w)$ in Cartesian coordinates (x, y, z) with z in the upward vertical direction. Dropping the tildes and assuming the Boussinesq approximation

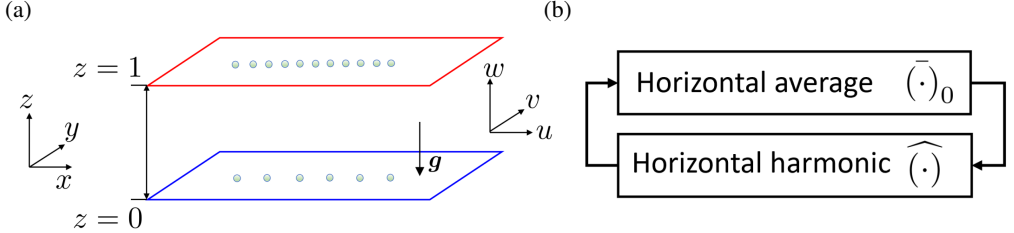


Figure 1: (a) The salt-finger convection setup. The red color indicates a hot plate while the blue color suggests a cold plate. The number of circles on top and bottom plates suggests the salinity at the top is higher than at the bottom. (b) Nonlinear interaction within the single-mode equations (2.7): horizontal averages $(\cdot)_0$ influence the horizontal harmonics $(\cdot̂)$ through (2.7a)-(2.7d), while the horizontal harmonics $(\cdot̂)$ contribute to the horizontal averages $(\cdot)_0$ through (2.7e)-(2.7g).

the system is governed by

$$\partial_t \mathbf{u} + \mathbf{u} \cdot \nabla \mathbf{u} = Pr \nabla^2 \mathbf{u} - \nabla p + Pr Ra_T (T - R_\rho^{-1} S) \mathbf{e}_z, \quad (2.2a)$$

$$\nabla \cdot \mathbf{u} = 0, \quad (2.2b)$$

$$\partial_t T + \mathbf{u} \cdot \nabla T + w = \nabla^2 T, \quad (2.2c)$$

$$\partial_t S + \mathbf{u} \cdot \nabla S + w = \tau \nabla^2 S. \quad (2.2d)$$

Here p is the dimensionless pressure $p = p_* h^2 / \kappa_T^2 \rho_{r*}$ while \mathbf{e}_z in (2.2a) is the unit vector in the vertical direction associated with buoyancy. The governing parameters include the Prandtl number, the diffusivity ratio, the density ratio, and the thermal Rayleigh number defined by:

$$Pr := \frac{\nu}{\kappa_T}, \quad \tau := \frac{\kappa_S}{\kappa_T}, \quad R_\rho := \frac{\alpha \Delta T}{\beta \Delta S}, \quad Ra_T := \frac{g \alpha \Delta T h^3}{\kappa_T \nu}, \quad (2.3a-d)$$

where ν is the viscosity and κ_S is the salinity diffusivity.

We impose constant temperature and salinity as boundary conditions at the top and the bottom plates:

$$T(x, y, z = 0, t) = T(x, y, z = 1, t) = 0, \quad (2.4a)$$

$$S(x, y, z = 0, t) = S(x, y, z = 1, t) = 0, \quad (2.4b)$$

while for the velocity we adopt no-slip boundary conditions:

$$\mathbf{u}(x, y, z = 0, t) = \mathbf{u}(x, y, z = 1, t) = 0. \quad (2.5)$$

Periodic boundary conditions in the horizontal are imposed on all variables.

We next formulate single-mode equations following the procedure in Herring (1963, 1964); Gough *et al.* (1975); Gough & Toomre (1982); Paparella & Spiegel (1999); Paparella *et al.* (2002). The single-mode ansatz is

$$S(x, y, z, t) = \bar{S}_0(z, t) + \hat{S}(z, t) e^{i(k_x x + k_y y)} + c.c., \quad (2.6a)$$

$$T(x, y, z, t) = \bar{T}_0(z, t) + \hat{T}(z, t) e^{i(k_x x + k_y y)} + c.c., \quad (2.6b)$$

$$\mathbf{u}(x, y, z, t) = \bar{\mathbf{U}}_0(z, t) \mathbf{e}_x + \hat{\mathbf{u}}(z, t) e^{i(k_x x + k_y y)} + c.c., \quad (2.6c)$$

$$p(x, y, z, t) = \bar{P}_0(z, t) + \hat{p}(z, t) e^{i(k_x x + k_y y)} + c.c., \quad (2.6d)$$

where c.c. denotes the complex conjugate. Equation (2.6a) decomposes the departure of the

salinity from the linear profile into a horizontally averaged quantity $\bar{S}_0(z, t)$ and a single harmonic in the horizontal direction associated with the wavenumber pair (k_x, k_y) and characterized by the complex amplitude $\hat{S}(z, t)$. The temperature is decomposed similarly. To allow for mean flow in the horizontal we decompose the velocity into a large-scale shear $\bar{U}_0(z, t)\mathbf{e}_x$ and a harmonic associated with the same wavenumber pair (k_x, k_y) as in equation (2.6c). The horizontally averaged vertical velocity is zero based on the continuity equation (2.2b) and the boundary conditions $w(z = 0) = w(z = 1) = 0$. The horizontally averaged quantities $(\bar{\cdot})_0$ are real and the amplitudes of the horizontal harmonics $(\hat{\cdot})$ are in general complex. Equations (2.6) assume a horizontal planform in the form of square cells, an assumption that also includes 2D rolls when $k_y = 0$. Other planforms such as hexagons generate additional self-interaction terms in the single-mode equations (Gough *et al.* 1975) and we leave this extension to future work.

We now substitute (2.6) into the governing equations (2.2), dropping all harmonics beyond the first, and balance separately the horizontally averaged components and the harmonic components. We eliminate the horizontally averaged pressure via $-\partial_z \bar{P}_0 + Pr Ra_T (\bar{T}_0 - R_\rho^{-1} \bar{S}_0) = 0$ and eliminate the harmonic component of the pressure using the continuity equation (2.2b). The resulting single-mode equations can then be expressed in terms of the vertical velocity w and vertical vorticity $\zeta := \partial_y u - \partial_x v$:

$$\partial_t \hat{\nabla}^2 \hat{w} + ik_x \bar{U}_0 \hat{\nabla}^2 \hat{w} - ik_x \bar{U}_0'' \hat{w} = Pr \hat{\nabla}^4 \hat{w} + Pr \hat{\nabla}_\perp^2 Ra_T (\hat{T} - R_\rho^{-1} \hat{S}), \quad (2.7a)$$

$$\partial_t \hat{\zeta} + ik_x \bar{U}_0 \hat{\zeta} + ik_y \bar{U}_0' \hat{w} = Pr \hat{\nabla}^2 \hat{\zeta}, \quad (2.7b)$$

$$\partial_t \hat{T} + ik_x \bar{U}_0 \hat{T} + \hat{w} \partial_z \bar{T}_0 + \hat{w} = \hat{\nabla}^2 \hat{T}, \quad (2.7c)$$

$$\partial_t \hat{S} + ik_x \bar{U}_0 \hat{S} + \hat{w} \partial_z \bar{S}_0 + \hat{w} = \tau \hat{\nabla}^2 \hat{S}, \quad (2.7d)$$

$$\partial_t \bar{U}_0 + \partial_z (\hat{w}^* \hat{u} + \hat{w} \hat{u}^*) = Pr \partial_z^2 \bar{U}_0, \quad (2.7e)$$

$$\partial_t \bar{T}_0 + \partial_z (\hat{w}^* \hat{T} + \hat{w} \hat{T}^*) = \partial_z^2 \bar{T}_0, \quad (2.7f)$$

$$\partial_t \bar{S}_0 + \partial_z (\hat{w}^* \hat{S} + \hat{w} \hat{S}^*) = \tau \partial_z^2 \bar{S}_0, \quad (2.7g)$$

$$\hat{u} = \frac{ik_x \partial_z \hat{w}}{k_x^2 + k_y^2} - \frac{ik_y}{k_x^2 + k_y^2} \hat{\zeta}, \quad (2.7h)$$

where the superscript * denotes a complex conjugate and $\hat{\nabla}^2 := \partial_z^2 - k_x^2 - k_y^2$, $\hat{\nabla}_\perp^2 := -k_x^2 - k_y^2$, $\hat{\nabla}^4 := \partial_z^4 - 2(k_x^2 + k_y^2) \partial_z^2 + (k_x^2 + k_y^2)^2$, $\bar{U}_0' := \partial_z \bar{U}_0$ and $\bar{U}_0'' := \partial_z^2 \bar{U}_0$. The corresponding boundary conditions for the salinity and temperature are:

$$\hat{S}(z = 0, t) = \hat{S}(z = 1, t) = \hat{T}(z = 0, t) = \hat{T}(z = 1, t) \quad (2.8a)$$

$$= \bar{S}_0(z = 0, t) = \bar{S}_0(z = 1, t) = \bar{T}_0(z = 0, t) = \bar{T}_0(z = 1, t) \quad (2.8b)$$

$$= 0, \quad (2.8c)$$

while the no-slip boundary conditions in (2.5) correspond to

$$\hat{w}(z = 0, t) = \hat{w}(z = 1, t) = \partial_z \hat{w}(z = 0, t) = \partial_z \hat{w}(z = 1, t) \quad (2.9a)$$

$$= \hat{\zeta}(z = 0, t) = \hat{\zeta}(z = 1, t) = \bar{U}_0(z = 0, t) = \bar{U}_0(z = 1, t) \quad (2.9b)$$

$$= 0. \quad (2.9c)$$

Equations (2.7a)-(2.7d) are the governing equation for the first harmonic in the presence of the large-scale fields \bar{U}_0 , \bar{T}_0 and \bar{S}_0 . In particular, equation (2.7a) is the Orr-Sommerfeld equation modified by an additional buoyancy term, while (2.7b) is known as the Squire

Symmetry name	Formulation	Primitive equations in (2.2)	Single-mode in (2.7)
Midplane reflection	$z \rightarrow 1 - z$ $(w, T, S) \rightarrow -(w, T, S)$	$(\hat{w}, \hat{T}, \bar{T}_0, \hat{S}, \bar{S}_0) \rightarrow -(\hat{w}, \hat{T}, \bar{T}_0, \hat{S}, \bar{S}_0)$	$z \rightarrow 1 - z$ $(\hat{w}, \hat{T}, \bar{T}_0, \hat{S}, \bar{S}_0) \rightarrow -(\hat{w}, \hat{T}, \bar{T}_0, \hat{S}, \bar{S}_0)$
Horizontal reflection	$x \rightarrow -x$ $u \rightarrow -u$		$k_x \rightarrow -k_x$ $(\hat{u}, \bar{U}_0, \hat{\zeta}) \rightarrow -(\hat{u}, \bar{U}_0, \hat{\zeta})$
Horizontal translation	$x \rightarrow x + \delta x$		$(\cdot) \rightarrow (\cdot)e^{ik_x \delta x}$

Table 1: Symmetry properties of the primitive equations in (2.2) and the single-mode equations in (2.7).

equation for the vertical vorticity (Schmid & Henningson 2012). Note that the large-scale shear \bar{U}_0 is self-induced (i.e., a variable to be solved for) instead of an imposed background shear. Thus the terms involving \bar{U}_0 in equations (2.7a)-(2.7d) are also *nonlinear*. The remaining equations (2.7e)-(2.7g) are the governing equations for the horizontally averaged quantities, distorted by the harmonic fluctuations. The resulting nonlinear interaction between horizontally averaged quantities and horizontal harmonics is summarized schematically in figure 1(b). Equation (2.7h) is used to obtain the horizontal velocity \hat{u} from the \hat{w} and $\hat{\zeta}$ required for the computation of the Reynolds stress in (2.7e).

Similar single-mode equations were previously used to study double-diffusive convection focusing on the diffusive regime; see, e.g., Gough & Toomre (1982, equations (3.7)-(3.11)), but did not include the coupling to the large large-scale shear \bar{U}_0 . A numerical simulation of the same single-mode equation in a 2D configuration (i.e., with $k_y = 0$) and stress-free boundary conditions was employed to study double-diffusive convection in both the fingering regime (Paparella & Spiegel 1999) and the diffusive regime (Paparella *et al.* 2002).

Here we focus on the bifurcation properties of the single-mode equations (2.7). These reflect the symmetries of the primitive equations (2.2), including midplane reflection, horizontal reflection, and horizontal translation, as summarized in table 1. Note that we arbitrarily assume that the large-scale shear \bar{U}_0 is generated in the x -direction within the single-mode equations (2.7). This is appropriate in a 2D configuration, but in 3D the large-scale shear can be oriented in principle in any horizontal direction, a possibility that is also left for future work.

In the following we perform bifurcation analysis using pde2path (Uecker *et al.* 2014; Uecker 2021a) to obtain nonlinear solution profiles and analyze their stability. The vertical direction is discretized using the Chebyshev differentiation matrix (Weideman & Reddy 2000) implemented following Uecker (2021b). The number of grid points used, including the boundary, range from $N_z = 65$ for results at $R_\rho = 40$ to $N_z = 257$ for results at $R_\rho = 2$; our continuation in R_ρ also uses $N_z = 257$ grid points. The tolerance of the maximal absolute value of the residue over each vertical location (L_∞ norm) is set as 10^{-6} . The horizontal translation symmetry within the single-mode equations requires an additional phase condition to robustly fix the phase and obtain a unique solution, and is implemented following Rademacher & Uecker (2017). The stability of each solution is examined via the eigenvalues of the associated Jacobian matrix. For validation we reproduced the results for single-mode equations for Rayleigh-Bénard convection (Herring 1963, 1964; Toomre

et al. 1977), as well as the high wavenumber asymptotic single-mode equations for Rayleigh-Bénard convection (Bassom & Zhang 1994, section 3) and porous medium convection (Lewis *et al.* 1997, section 3). Selected solution profiles obtained from pde2path were also validated against the results obtained from the nonlinear boundary value problem (NLBVP) solver in Dedalus (Burns *et al.* 2020), and selected eigenvalue computations from pde2path are also consistent with the eigenvalue problem (EVP) solver in Dedalus (Burns *et al.* 2020). Finally, selected predictions from the bifurcation diagram and stability properties (figure 18(a)) were also validated against direct numerical simulations (IVP solver) of the single-mode equations (2.7) using Dedalus (Burns *et al.* 2020).

We also performed 2D direct numerical simulations (DNS) of the primitive equations (2.2) using Dedalus (Burns *et al.* 2020) to further analyze the accuracy and stability of the solutions obtained from the bifurcation analysis of the single-mode equations. We focus on 2D domains with periodic boundary conditions in the horizontal and the no-slip boundary conditions (2.5) in the vertical direction. We use a Chebyshev spectral method in the vertical direction with $N_z = 128$ grid points with a Fourier spectral method in the horizontal direction with $N_x = 128$ and a dealiasing scaling factor 3/2. To check the accuracy we doubled the number of grid points in both x and z directions for selected results and confirmed that the resulting Sherwood number Sh in figure 16 (steady rolls resembling the S1 solution) does not change up to eight decimal places. Time is advanced using a 3rd-order 4-stage diagonal implicit Runge-Kutta (DIRK) scheme coupled with a 4-stage explicit Runge-Kutta (ERK) scheme (RK443) (Ascher *et al.* 1997, section 2.8). We mention that we do not expect the DNS results to coincide in all cases with the single-mode results. This is because the former include, in principle, all spatial harmonics of the fundamental wavenumber; it is precisely these that are omitted from the single-mode theory. We are interested in identifying parameter regimes in which the single-mode theory provides quantitatively accurate results as well as regimes in which it fails. In all cases, the horizontal domain is selected based on the wavenumber employed in constructing the single-mode solutions, as described in detail in the next section.

3. Single-mode solutions and stability at $Pr = 7$

We start with the results for $Pr = 7$, a Prandtl number value appropriate to oceanographic applications, and fix $\tau = 0.01$, corresponding to the diffusivity ratio between salinity and temperature. The thermal Rayleigh number is fixed at $Ra_T = 10^5$ for a direct comparison with DNS results (Yang *et al.* 2015, 2016a). Table 2 provides a summary of the solutions, all of which are described in more detail below. All the solutions in the table are steady-state solutions, including the traveling waves (TW1) which are computed as steady states in a frame moving with the phase speed c of the wave. This speed solves a nonlinear eigenvalue problem. The bifurcation diagrams presented in this work (figures 2, 10, 13, 16 and 18) all show the time-averaged Sherwood number Sh as a function of the horizontal domain size L_x or equivalently the fundamental wavenumber $k_x = 2\pi/L_x$, where

$$Sh := \langle \partial_z S |_{z=0} \rangle_{h,t} + 1 \quad (3.1)$$

with $\langle \cdot \rangle_{h,t}$ indicating average in both the horizontal direction and over time. Without confusion, $\langle \cdot \rangle_{h,t}$ is also referred to as a *mean*. In particular, for steady-state single-mode solutions, we obtain

$$Sh = \langle \partial_z \bar{S}_0 |_{z=0} \rangle_t + 1 = \partial_z \bar{S}_0 |_{z=0} + 1, \quad (3.2)$$

Abbreviation	Description	Bifurcate from	Stability	$\bar{U}_0(z)$	Color
S1	Symmetric one-layer solutions	Trivial	S/U	= 0	Black (—)
S2	Symmetric two-layer solutions	Trivial	U	= 0	Red (—)
S3	Symmetric three-layer solutions	Trivial	U	= 0	Blue (—)
TF1	Tilted fingers	S1	S/U	$\neq 0$	Magenta (—)
TW1	Traveling waves	S1	S/U	$\neq 0$	Green (—)
A2	Asymmetric two-layer solutions	S2	U	= 0	Cyan (—)
A3	Asymmetric three-layer solutions	S3	U	= 0	Brown (—)

Table 2: Summary of solution features, stability, induced large-scale shear $\bar{U}_0(z)$ and line color employed in the bifurcation diagrams (figures 2, 10, 13, 16 and 18). Symmetry is with respect to mid-plane reflection. S/U indicates both stable and unstable solutions exist along this solution branch and U indicates that only unstable solutions were found.

where $\langle \cdot \rangle_t$ denotes time-averaging. We also use $\langle \cdot \rangle_h$ to denote averaging in the horizontal. For time-dependent solutions such as those obtained from DNS, these two types of averaging yield distinct results.

In the bifurcation diagrams reported below, we use thick lines to indicate stable solutions while thin lines represent unstable solutions. When the maximum amplitude of the large-scale shear mode $\max_z |\bar{U}_0(z)|$ along a branch is of the order of machine precision or smaller we report it as zero (see table 2). In all other cases $\bar{U}_0(z) \neq 0$. When the large-scale shear is not generated, $\bar{U}_0 = 0$, the harmonic quantities $\hat{w}(z, t)$, $\tilde{u}(z, t) := -i\hat{u}(z, t)$, $\hat{S}(z, t)$ and $\hat{T}(z, t)$ are real for a suitably chosen phase. For solutions associated with an induced large-scale shear $\bar{U}_0 \neq 0$, we report both real and imaginary parts of the harmonic profile denoted by $\mathcal{Re}[\cdot]$ and $\mathcal{Im}[\cdot]$, respectively. We refer to the base state in which all variables within the single-mode theory vanish as the trivial state. This state corresponds to $Sh = 1$. Except for the results with stress-free velocity boundary conditions in subsection 3.2, all our results are computed for no-slip boundary conditions.

3.1. Solution profiles and comparison with DNS at $R_\rho = 40$

We start from the dynamics near onset when $R_\rho = 40$, i.e., for $R_\rho\tau \sim O(1)$. This is the parameter regime close to the onset of salt-finger instability with $R_{\rho,\text{crit}} = 1/\tau$ in vertically periodic domains (Radko 2013, equation (2.4)) previously studied by Radko & Stern (1999, 2000) and Xie *et al.* (2017, 2019). The main challenge of the single-mode approach is the correct choice of the horizontal wavenumber k_x , cf. Toomre *et al.* (1977). As a result, we start by analyzing the bifurcation diagram as a function of k_x and compare the results with DNS in domains of length $L_x = 2\pi/k_x$. This approach provides insight into the effects of the domain size.

Figure 2 shows the bifurcation diagram at $R_\rho = 40$ with no-slip boundary conditions. We consider both 2D results with $k_y = 0$ in figure 2(a) and 3D results with $k_y = k_x$ in figure 2(b) indicating the same aspect ratio in two different horizontal directions (x and y). Here, these two bifurcation diagrams show almost the same behavior, and we can transform the 3D results in figure 2(b) by defining an equivalent 2D horizontal wavenumber

$$k_{x,2D} = \sqrt{k_x^2 + k_y^2} \quad (3.3)$$

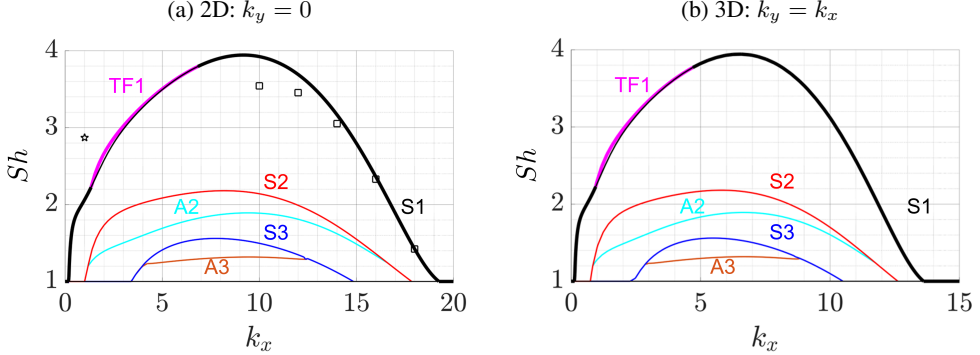


Figure 2: Bifurcation diagrams as a function of the fundamental wavenumber k_x from the single-mode equations (2.7) for (a) 2D: $k_y = 0$, (b) 3D: $k_y = k_x$, and the parameters $R_\rho = 40$, $Pr = 7$, $\tau = 0.01$, $Ra_T = 10^5$. The black squares show the Sh of the steady state reached using 2D DNS in domains of size $L_x = 2\pi/k_x$ (table 3); the black pentagram corresponds to DNS with $L_x = 2\pi$ displaying persistent chaotic behavior.

to obtain the same 2D results as in figure 2(a). This suggests that in this parameter regime, the 2D and 3D results are close to one another after a rescaling of the horizontal domain and wavenumber. This can be readily seen from the single-mode equation (2.7) where the horizontal wavenumbers always appear as $k_x^2 + k_y^2$ when a large-scale shear is not generated, i.e., $\bar{U}_0 = 0$.

The solutions S1, S2 and S3 all bifurcate from the trivial solution. The S1, S2 and S3 solution profiles with $k_x = 8$, $k_y = 0$ are shown in figure 3. The horizontally averaged total salinity profiles $z + \bar{S}_0(z)$ in figure 3(a) show that these solutions are, respectively, associated with one, two and three relatively well-mixed regions. These solution profiles thus resemble the staircases observed in field measurements, e.g., (Schmitt *et al.* 1987). Staircase-like solutions are also shown in some snapshots from direct numerical simulations (Piacsek & Toomre 1980, figure 2) and reproduced by Zhang *et al.* (2018, figure 3). Recent DNS results show the coexistence of multiple states with one, two, or three well-mixed regions using different initial conditions (Yang *et al.* 2020, figure 2). In all three cases the well-mixed regions correspond to large values of the salinity amplitude \hat{S} as shown in figure 3(b), as well as a large vertical velocity \hat{w} as shown in figure 3(d). In contrast, the horizontal velocity peaks outside of the well-mixed region in each solution.

The second row of figure 3 reconstructs the total salinity using equations (2.6a) and (2.1), while the third row of figure 3 shows the isocontours of the 2D streamfunction computed as $\psi(x, z) = \bar{\psi}_0(z) + \hat{\psi}(z)e^{ik_x x} + c.c.$ with $\bar{\psi}_0(z) = -\int_0^z \bar{U}_0(\xi)d\xi$ and $\hat{\psi} = \hat{w}/(ik_x)$. The isocontours are equispaced between ± 0.9 of the maximum value. The line (—) is used for positive (clockwise) streamlines while (—, blue) indicates negative (counterclockwise) streamlines throughout this work. These results suggest that each well-mixed region is associated with one downward and one upward moving plume. Since salinity tends to be homogenized in regions of closed steady streamlines (Rhines & Young 1983) while salinity gradients are expelled from these regions, the resulting mean salinity exhibits an overall staircase-like profile.

Previous analysis of salt-finger convection in the spirit of single-mode solutions (Radko & Stern 2000; Proctor & Holyer 1986) also found the S1 type of solution, but S2 and S3 solutions were not found. This is likely because these studies (Radko & Stern 2000; Proctor & Holyer 1986) focused on the asymptotic behavior close to the onset of instability but did not go beyond the first bifurcation point from the trivial solution.

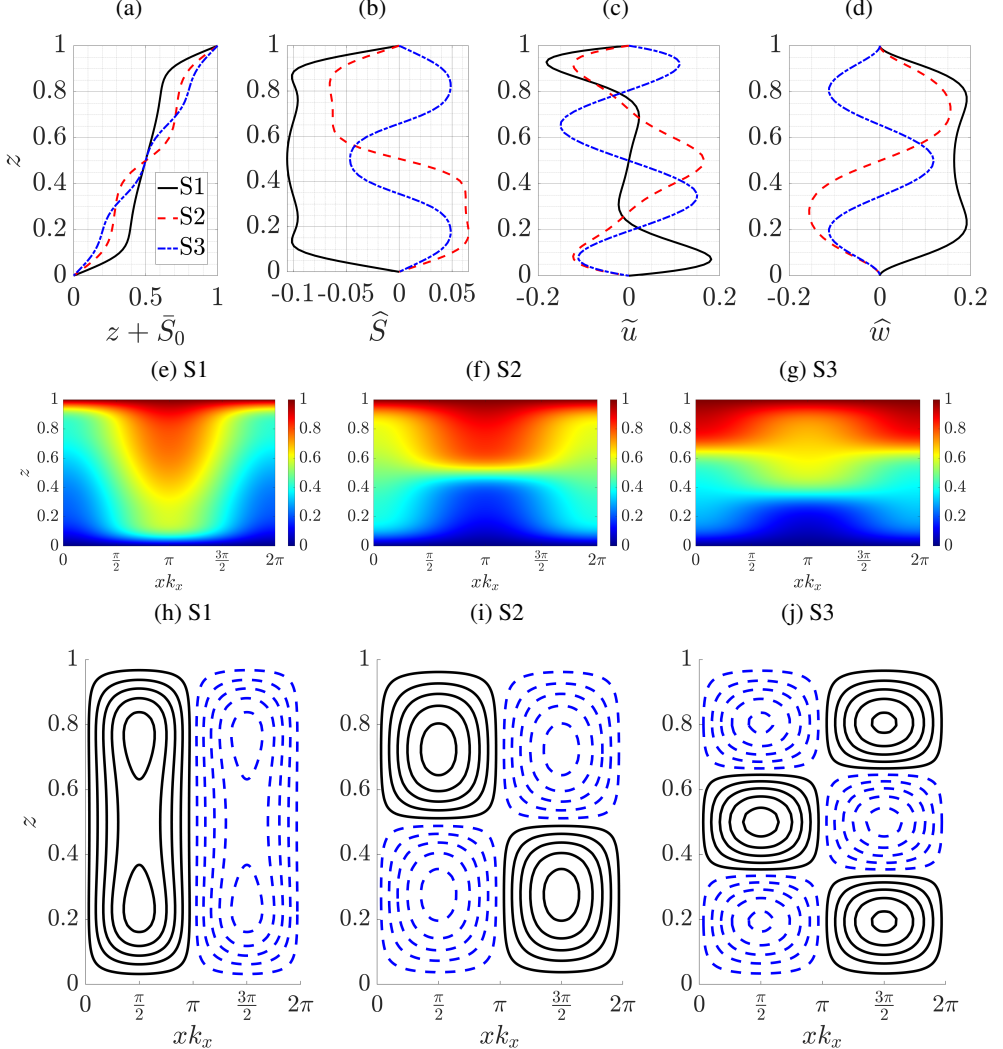


Figure 3: Solution profiles from the single-mode equations (2.7) in the form of S1, S2 and S3 when $k_x = 8$, $k_y = 0$, $R_\rho = 40$, $Pr = 7$, $\tau = 0.01$, $Ra_T = 10^5$. The first row shows the profiles of (a) $z + \bar{S}_0$, (b) \hat{S} , (c) \tilde{u} , and (d) \hat{w} . The second row shows the reconstructed total salinity using (2.6a) and (2.1) for (e) S1, (f) S2 and (g) S3 solutions. The third row shows isocontours of the streamfunction for (h) S1, (i) S2 and (j) S3 solutions.

We also examined secondary bifurcations of the solutions S1, S2, and S3 in figure 2(a), focusing on the bifurcation points closest to their high wavenumber onset. The resulting secondary branches are of two types, corresponding to tilted fingers (TF1) and asymmetric layer spacing (A2 and A3). These states break the left-right reflection and the midplane reflection symmetry, respectively, as revealed by the corresponding solution profiles shown in figures 4 and 5. The mean salinity profile $z + \bar{S}_0$ for TF1 in figure 4(a) is associated with two relatively well-mixed regions near $z \in [0.2, 0.4]$ and $z \in [0.6, 0.8]$, while in the interior $z \in [0.4, 0.6]$ the profile is close to linear. The corresponding profile of \hat{S} in figure 4(b) has both real and imaginary components with even and odd symmetry with respect to the midplane, respectively, indicating that the harmonics are no longer in phase in the vertical.

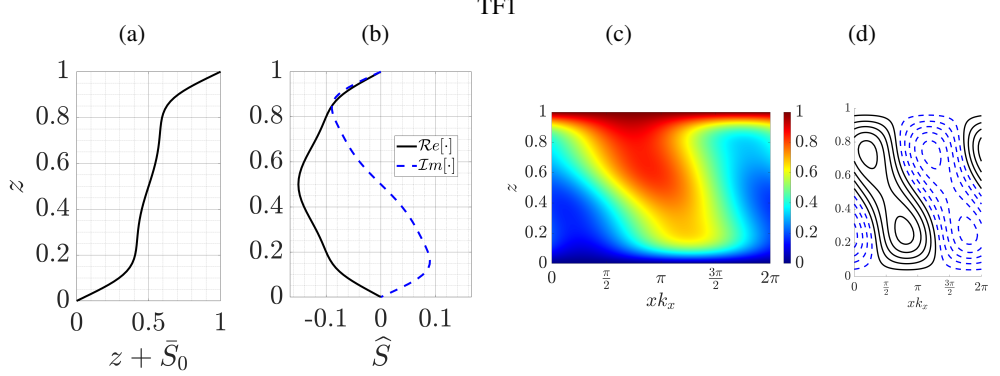


Figure 4: Solution profiles of the TF1 state from the single-mode equations (2.7) with $k_x = 4$, $k_y = 0$, $R_\rho = 40$, $Pr = 7$, $\tau = 0.01$, $Ra_T = 10^5$. Panels (a) and (b) show the profiles of $z + \bar{S}_0$ and \hat{S} , respectively, while (c) and (d) show the reconstructed total salinity using (2.6a) and (2.1) and the isocontours of the streamfunction.

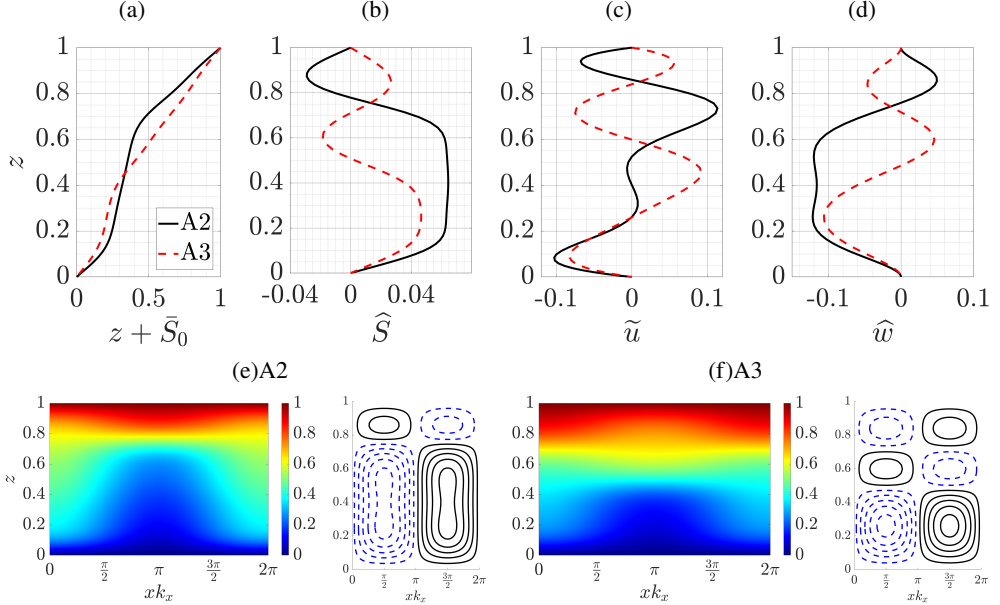


Figure 5: Solution profiles of the A2 and A3 states from the single-mode equations (2.7) with $k_x = 8$, $k_y = 0$, $R_\rho = 40$, $Pr = 7$, $\tau = 0.01$, $Ra_T = 10^5$. The first row shows the profiles of (a) $z + \bar{S}_0$, (b) \hat{S} , (c) \tilde{u} and (d) \tilde{w} . The second row shows the reconstructed total salinity using (2.6a) and (2.1) and the isocontours of the streamfunction for (e) A2, (f) A3.

The reconstructed total salinity shown in figure 4(c) reveals that the finger is now tilted; see also the streamfunction shown in figure 4(d). The tilted finger generates a nonzero large-scale shear with $\max_z \bar{U}_0(z) = 3.16 \times 10^{-4}$. The profile of the large-scale shear is shown farther below (figures 15(a) and 19(b)) for parameter values for which it is much stronger. A similar tilted finger state accompanied by large-scale shear was observed in earlier simulations of the single-mode equations (Paparella & Spiegel 1999) and reported in observations from the North Atlantic Tracer Release Experiment (St. Laurent & Schmitt 1999, figure 3) as well as in laboratory experiments on salt-finger convection; see, e.g., Taylor & Bucens (1989, figure

2) and Krishnamurti (2009, figure 2). A related mechanism has also been widely reported in experiments on Rayleigh-Bénard convection (Krishnamurti & Howard 1981) as well as in direct numerical simulations of 2D Rayleigh-Bénard convection (Goluskin *et al.* 2014); see the review by Siggia (1994).

The solution profiles in figures 5(a)-(d) indicate that the A2 and A3 solutions spontaneously break the midplane reflection symmetry; states obtained via reflection in the midplane are therefore also solutions. In particular, the profile $z + \bar{S}_0(z)$ no longer passes through $(1/2, 1/2)$. However, the reconstructed total salinity profile and the isocontours of the streamfunction in figures 5(e)-(f) still resemble, qualitatively, the S2 and S3 profiles that distinguish these two asymmetric solutions. In particular, the A2 streamlines show two counter-rotating but unequal rolls in the vertical while the A3 solution exhibits three counter-rotating rolls, much as in the S2 and S3 states shown in figures 3(i)-(j). Solutions that are asymmetric with respect to midplane reflection have been seen in magnetohydroconvection with a depth-dependent magnetic diffusivity (Julien *et al.* 2000, figure 17) but are a consequence of forced symmetry breaking. Here, such asymmetric solutions originate from spontaneous symmetry breaking.

The stability of these solutions is indicated by thick (stable) and thin (unstable) lines in figure 2. Near onset, i.e., in the large or small wavenumber regime, S1 is stable and with the largest Sh among all the solutions shown in the figure, a finding that is broadly consistent with the ‘relative stability’ criterion of Malkus & Veronis (1958).

The dynamics of unstable solutions are typically not easy to isolate and analyze without suitable initial conditions. Here, we use our single-mode solutions as initial conditions for DNS to provide additional insight into their stability. We set the horizontal domain size as $L_x \in [2\pi/18, 4\pi]$ and then use the single-mode solution profile at $k_x = 2\pi/L_x$, $k_y = 0$, to construct a 2D initial condition using the ansatz in (2.6). The final state after $t = 3000$ for different L_x and initial conditions based on S1, S2, S3, and TF1 solutions is summarized in table 3. For small horizontal domains ($L_x \leq 2\pi/10$) the domain constrains the finger to be tall and thin and the DNS results with S1, S2, and S3 initial conditions all transition to a solution resembling the one-layer solution S1. This is consistent with the stability observation in the bifurcation diagram in figure 2. The DNS also provides the final Sh numbers and these values are plotted using black squares in figure 2(a). The predicted Sh from the single-mode solution is close to the DNS results, especially close to the high wavenumber onset of the S1 solution ($k_x = 19.251$). The accuracy of the single-mode equations close to the high wavenumber onset is a consequence of the strong damping of modes with wavenumbers $k_x = 2\pi n/L_x$ ($n \in \mathbb{Z}$ and $n \geq 2$, e.g., $k_x = 4\pi/L_x$, $k_x = 6\pi/L_x$) that leaves only the trivial solution at these wavenumbers (see figure 2).

The final states in a domain of size $L_x = 2\pi/8$ initialized by S2 and S3 show different flow structures. Figure 6 shows DNS results initialized with S2 and $L_x = 2\pi/8$. The horizontally averaged salinity deviation $\langle S \rangle_h(z, t)$ in figure 6(a) takes the requisite two-layer form for short times but then transitions into a one-layer state with superposed oscillations in time. After averaging over time and in the horizontal direction, the total salinity profile $z + \langle S \rangle_{h,t}$ in figure 6(b) shows two well-mixed regions, with a broad interior region that is close to a linear profile. This behavior is similar to the TF1 single-mode solution as shown in figure 4(a). The mean salinity profile in figure 6(b) also resembles the mean temperature profile in Rayleigh-Bénard convection with induced large-scale shear (Goluskin *et al.* 2014, figure 5(b)), where the temperature profile shows two well-mixed regions close to the boundary, and an interior that approaches a linear profile with increasing Rayleigh number. The three snapshots of the total salinity in figure 6(c)-(e) reveal that this behavior is associated with a new state, a direction-reversing tilted finger (RTF). Such behavior is also observed within simulations of the single-mode equations (Paparella & Spiegel 1999).

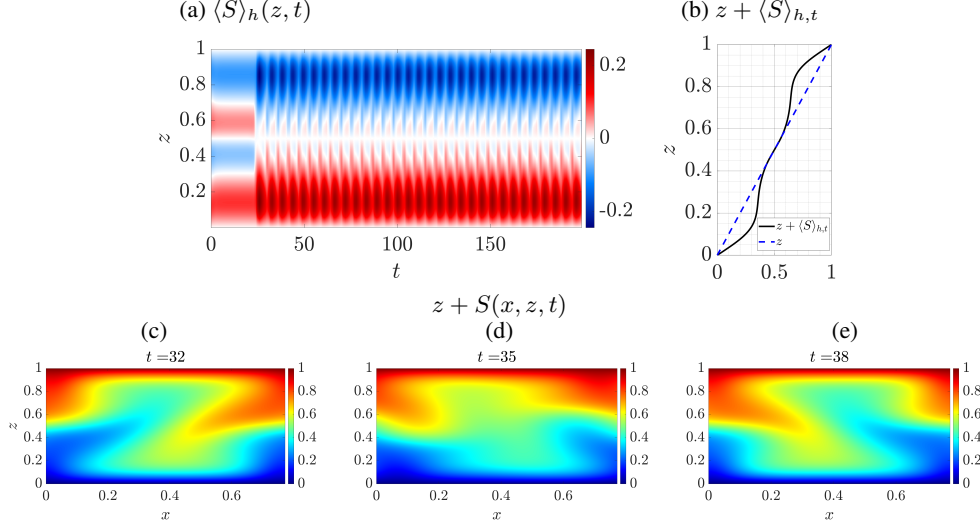


Figure 6: 2D DNS showing (a) horizontally averaged salinity $\langle S \rangle_h(z, t)$ and (b) time-averaged and horizontally averaged total salinity $z + \langle S \rangle_{h,t}$. The second row shows isocontours of the total salinity $z + S(x, z, t)$ at (c) $t = 32$, (d) $t = 35$, and (e) $t = 38$. The horizontal domain size is $L_x = 2\pi/8$ with initial condition in the form of a S2 single-mode solution with $k_x = 2\pi/L_x = 8$, $k_y = 0$. The parameters are $R_\rho = 40$, $Pr = 7$, $\tau = 0.01$, $Ra_T = 10^5$. See supplementary video 1.

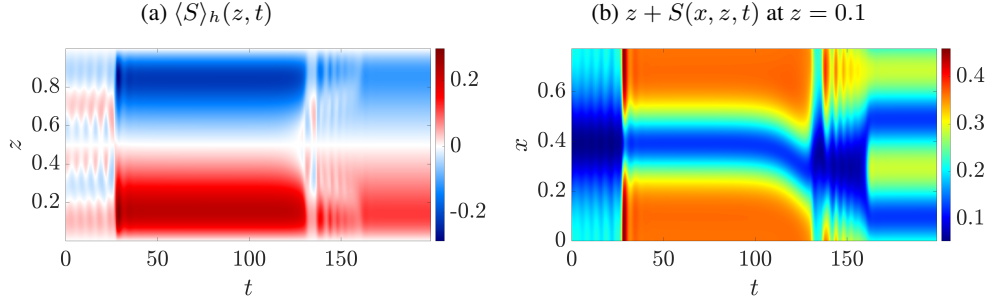


Figure 7: 2D DNS results showing (a) horizontally averaged salinity $\langle S \rangle_h(z, t)$ and (b) total salinity $z + S(x, z, t)$ at $z = 0.1$. The horizontal domain size is based on $L_x = 2\pi/8$ with S3 single-mode initial condition with $k_x = 2\pi/L_x = 8$, $k_y = 0$. The parameters are $R_\rho = 40$, $Pr = 7$, $\tau = 0.01$, $Ra_T = 10^5$. See supplementary video 2.

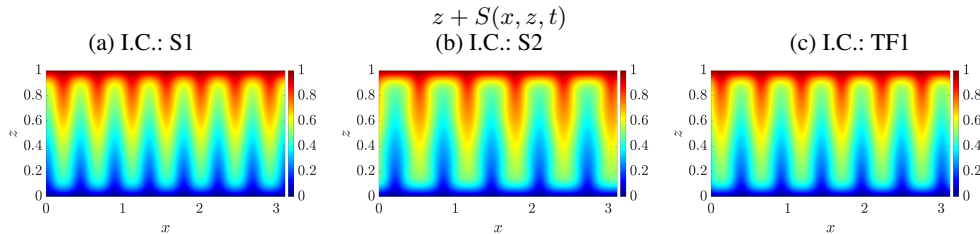


Figure 8: 2D DNS results for the total salinity $z + S(x, z, t)$ at $t = 3000$ in a horizontal domain of size $L_x = \pi$ initialized by (a) S1, (b) S2, and (c) TF1 single-mode solutions with $k_x = 2\pi/L_x = 2$, $k_y = 0$.

I.C.	L_x	2 π /18	2 π /16	2 π /14	2 π /12	2 π /10	2 π /8	2 π /6	2 π /4	2 π /2	2 π	4 π
S1	S1	S1	S1	S1	S1	S1 (2)	S1 (2)	S1 (3)	S1 (7)	C	C	
S2	-	S1	S1	S1	S1	RTF	S1 (2)	S1 (3)	S1 (5)	-	-	
S3	-	-	S1	S1	S1	S1 (2)	S1 (2)	S1 (3)	-	-	-	
TF1	-	-	-	-	-	-	S1 (2)	S1 (3)	S1 (6)	-	-	

Table 3: The flow structures of 2D DNS simulations at $t = 3000$ in domains of size L_x and initial condition (I.C.) constructed from S1, S2, S3 and TF1 solutions using the ansatz (2.6) with $k_x = 2\pi/L_x$, $k_y = 0$. RTF indicates direction-reversing tilted fingers and C represents chaotic behavior; ‘-’ indicates that a nonzero single-mode solution at $k_x = 2\pi/L_x$ is not present based on figure 2(a). The number $n \in \mathbb{Z}$ inside a bracket indicates that the final horizontal wavenumber reached by the solution is $k_x = 2\pi n/L_x$, $n > 1$, i.e. that the evolution results in a changed wavenumber.

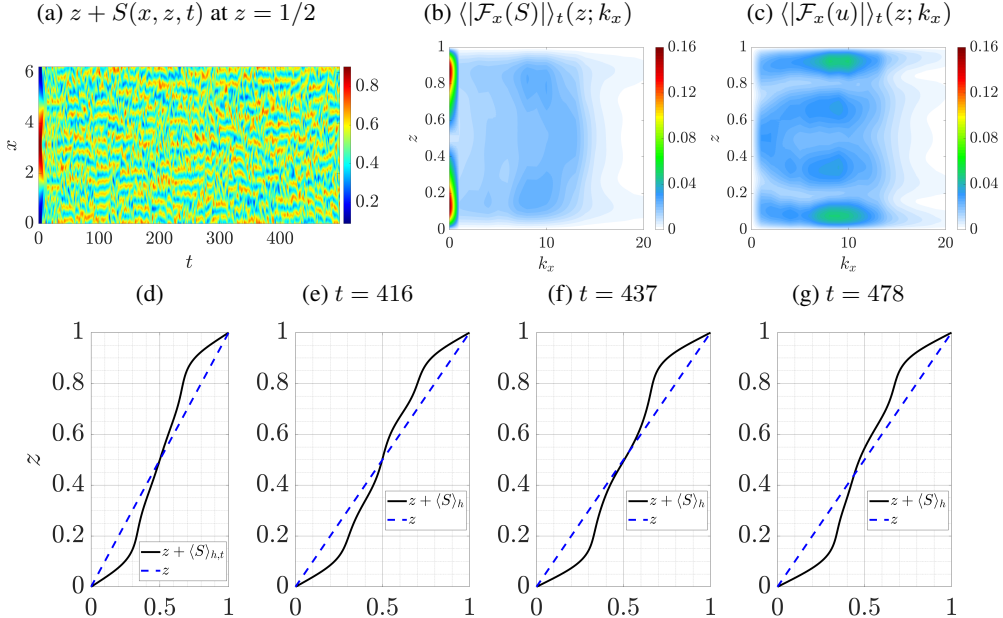


Figure 9: 2D DNS results displaying (a) total salinity $z + S(x, z, t)$ at $z = 1/2$, (b) $\langle |F_x(S)| \rangle_t(z; k_x)$, (c) $\langle |F_x(u)| \rangle_t(z; k_x)$, (d) $z + \langle S \rangle_{h,t}(z)$, and snapshots of the horizontally averaged total salinity $z + \langle S \rangle_h(z, t)$ at (e) $t = 416$, (f) $t = 437$ and (g) $t = 478$. The horizontal domain size is $L_x = 2\pi$ initialized by a S1 solution with $k_x = 2\pi/L_x = 1$, $k_y = 0$. The governing parameters are $R_\rho = 40$, $Pr = 7$, $\tau = 0.01$, and $Ra_T = 10^5$.

(termed a layering instability there) and is accompanied by an oscillating large-scale shear. The direction-reversing tilted finger state also resembles (at least phenomenologically) the ‘pulsating wave’ found by Proctor *et al.* (1994, figure 7) and Matthews *et al.* (1993, figure 5) in magnetoconvection. A comparison between convection with or without a stabilizing magnetic field also highlights the stabilizing restoring force that is important in sustaining

this ‘pulsating wave’ state (Rucklidge & Matthews 1996), here the stabilizing temperature gradient. We have not explored the origin of this state but note that similar ‘pulsating waves’ in other systems originate from a sequence of local and global bifurcations of a tilted convection roll (Matthews *et al.* 1993; Proctor *et al.* 1994; Rucklidge & Matthews 1996).

Figure 7 shows the DNS results with an S3 initial condition and $L_x = 2\pi/8$ and displays the dynamics that are typically involved in transitioning to a higher wavenumber S1 solution. The profile of $\langle S \rangle_h$ in figure 7(a) initially shows a three-layer structure but starts to oscillate prior to a transition to the one-layer state S1 at $t \approx 30$. After $t \approx 160$, this one-layer solution transitions to another one-layer solution but with a smaller magnitude in $\langle S \rangle_h$. The total salinity near the lower boundary, $z = 0.1$, is shown in figure 7(b) and further explains this transition scenario. The one-layer solution starts to tilt at $t \approx 110$ and begins to show oscillations at $t \approx 130$. Beyond $t \approx 160$, the horizontal wavenumber doubles leading to the S1(2) state in table 3. Such a transition to a higher wavenumber S1 solution is also observed with horizontal domains $L_x \in [2\pi/6, 2\pi/2]$, albeit with different possibilities for the final wavenumber. Note that such transitions between different horizontal wavenumbers are not possible within the single-mode approach.

For $L_x = \pi$, the final state shows different horizontal wavenumbers depending on the three different initial conditions S1, S2, and TF1 as indicated in table 3. The total salinity at $t = 3000$ in these three final states is shown in figure 8. Although the horizontal domain size and the governing parameters are the same, different initial conditions lead to different final horizontal wavenumbers and the DNS results suggest that these persist up to at least $t = 3000$. This observation suggests that these three different initial conditions S1, S2, and TF1 lie in the basin of attraction of S1 solutions associated with different and larger horizontal wavenumbers. This is of course a consequence of the preferred horizontal scale of the fingers. Rolls with different horizontal wavenumber obtained from different initial conditions are a familiar phenomenon in Rayleigh-Bénard convection (Wang *et al.* 2020) and in spanwise rotating plane Couette flow (Xia *et al.* 2018; Yang & Xia 2021).

Solutions that do not reach a well-organized structure will be referred to as chaotic. Such behavior is observed in large domains, e.g. $L_x = 2\pi$ and $L_x = 4\pi$. The total salinity in the midplane for $L_x = 2\pi$ is shown in figure 9(a), and displays chaotic behavior with multiple downward and upward plumes in the horizontal. In order to further characterize the horizontal length scale, we computed $\langle |\mathcal{F}_x(S)| \rangle_t(z; k_x)$ and $\langle |\mathcal{F}_x(u)| \rangle_t(z; k_x)$, where $\mathcal{F}_x(\cdot)$ is the Fourier transform in the x -direction and $|\cdot|$ represents the modulus of the obtained complex Fourier coefficients. The results are shown in figures 9(b)-(c). The $k_x = 0$ component of $\langle |\mathcal{F}_x(\cdot)| \rangle_t(z; k_x)$ is related to the amplitude of the horizontal mean $(\bar{\cdot})_0$ while the $k_x \neq 0$ contributions to $\langle |\mathcal{F}_x(\cdot)| \rangle_t(z; k_x)$ are associated with the harmonic components $(\widehat{\cdot})$ in the single-mode ansatz (2.6). Figure 9(b) displays a peak at $k_x = 0$ that corresponds to the deviation of the mean salinity from its linear profile. A second peak around $k_x \approx 9$ in figure 9(b) corresponds to a wavenumber that is close to that providing the largest Sh in the S1 solution shown in figure 2(a). However, in the midplane, the peak wavenumber shifts to $k_x = 13$. For the horizontal velocity, the plot of $\langle |\mathcal{F}_x(u)| \rangle_t$ in figure 9(c) also reveals a peak at $k_x = 9$ but now at multiple locations dominated by regions near the boundaries, with a lower amplitude near $z = 1/3$ and $2/3$, the peak region of horizontal velocity \tilde{u} in the three-layer solution S3 shown in figure 3(c). Furthermore, $\langle |\mathcal{F}_x(u)| \rangle_t$ also shows a local peak at $k_x = 1$ near the midplane, resembling the horizontal velocity \tilde{u} of the two-layer solution S2 shown in figure 3(c). These observations suggest that the unstable S2 and S3 solutions both play a role in the chaotic behavior and that their properties may manifest themselves in the statistics of the chaotic state, cf. Kawahara & Kida (2001) and the reviews by Kawahara *et al.* (2012) and Graham & Floryan (2021).

In order to further quantify the role of unstable solutions, we plot in figures 9(e)-(g) the horizontally averaged profiles at three different times for comparison with the horizontally averaged time-averaged state in figure 9(d). Although the salinity profile in the latter state does not show a significant staircase, the horizontally averaged salinity profiles at the three times shown in figures 9(e)-(f) do in fact show a tendency towards three and two steps, respectively, while the snapshot in figure 9(g) shows instead a salinity profile that temporarily breaks the midplane reflection symmetry. These results provide evidence that the chaotic state visits the neighborhood of not only the unstable staircase-like solutions S2 and S3 but also of the asymmetric solution. The time-averaged Sh within $t \in [100, 500]$ is $Sh \approx 2.8693$, a value lower than the maximal Sh for S1 but higher than those for S2 and S3 at the suggested peak wavenumber $k_x = 9$ as shown in figure 2(a), and suggests that these states may play a role in determining the time-averaged salinity transport in this chaotic state.

3.2. No-slip versus stress-free boundary conditions

Although no-slip boundary conditions are relevant for experiments (Hage & Tilgner 2010), stress-free boundary conditions are more appropriate for oceanographic applications. Here we compare the bifurcation diagram in the no-slip case with the corresponding diagram with stress-free boundary conditions. For this purpose we replace the original no-slip boundary conditions in (2.5) by the stress-free boundary conditions

$$w(x, y, z = 0, t) = w(x, y, z = 1, t) = 0, \quad (3.4a)$$

$$\partial_z u(x, y, z = 0, t) = \partial_z u(x, y, z = 1, t) = 0, \quad (3.4b)$$

$$\partial_z v(x, y, z = 0, t) = \partial_z v(x, y, z = 1, t) = 0. \quad (3.4c)$$

Within the single-mode equations, the corresponding velocity boundary conditions in (2.9) are thus replaced as:

$$\hat{w}(z = 0, t) = \hat{w}(z = 1, t) = \partial_z^2 \hat{w}(z = 0, t) = \partial_z^2 \hat{w}(z = 1, t) \quad (3.5a)$$

$$= \partial_z \hat{\zeta}(z = 0, t) = \partial_z \hat{\zeta}(z = 1, t) = \partial_z \bar{U}_0(z = 0, t) = \partial_z \bar{U}_0(z = 1, t) \quad (3.5b)$$

$$= 0. \quad (3.5c)$$

Note that the governing equations with stress-free boundary conditions admit an additional Galilean symmetry: the large-scale shear can be shifted by an arbitrary constant, $\bar{U}_0 \rightarrow \bar{U}_0 + C$. To obtain unique solutions we therefore impose the additional constraint $\int_0^1 \bar{U}_0(z, t) dz = 0$ following the procedure in Uecker (2021a, §6.9).

Figure 10 shows the resulting bifurcation diagram for comparison with figure 2. The diagrams are very similar: all of the previously discussed solution branches are still present. The main difference is that the stress-free boundary conditions typically lead to a larger Sh than the no-slip boundary conditions at the same horizontal wavenumber. This behavior is also consistent with the observation by Yang *et al.* (2016b), where 3D DNS results indicate that the flow morphology is qualitatively similar but stress-free boundary conditions display a larger Sh .

Figure 11 displays solution profiles and total salinity for the S1, S2 and S3 solutions at the same parameter values as in figure 3 but with stress-free instead of no-slip boundary conditions. Here, the horizontally averaged total salinity $z + \bar{S}_0$ still displays the one-layer, two-layer and three-layer solution profiles in vertical. The horizontal structure of these states is qualitatively similar to the no-slip results in figure 3. The main difference is that the horizontal velocity \tilde{u} and the gradient of vertical velocity $\partial_z \hat{w}$ no longer vanish at the boundaries.

Figure 12(a) displays the A2 and A3 solution profiles with stress-free boundary conditions.

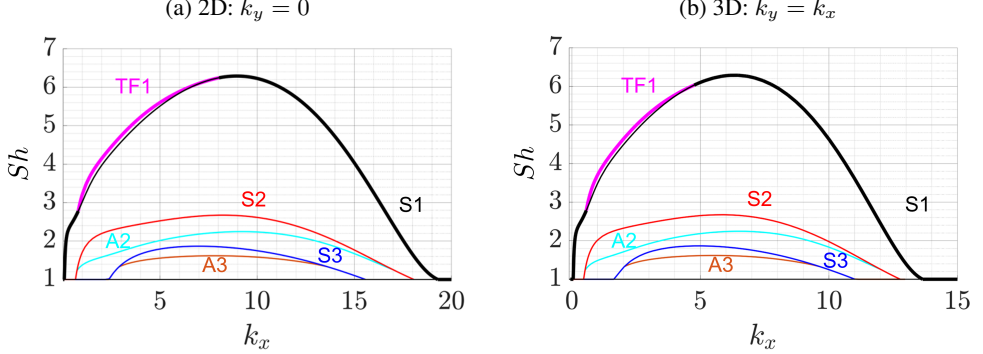


Figure 10: Bifurcation diagram computed from the single-mode equations (2.7) with the same parameter values as in figure 2 but stress-free velocity boundary conditions at top and bottom.

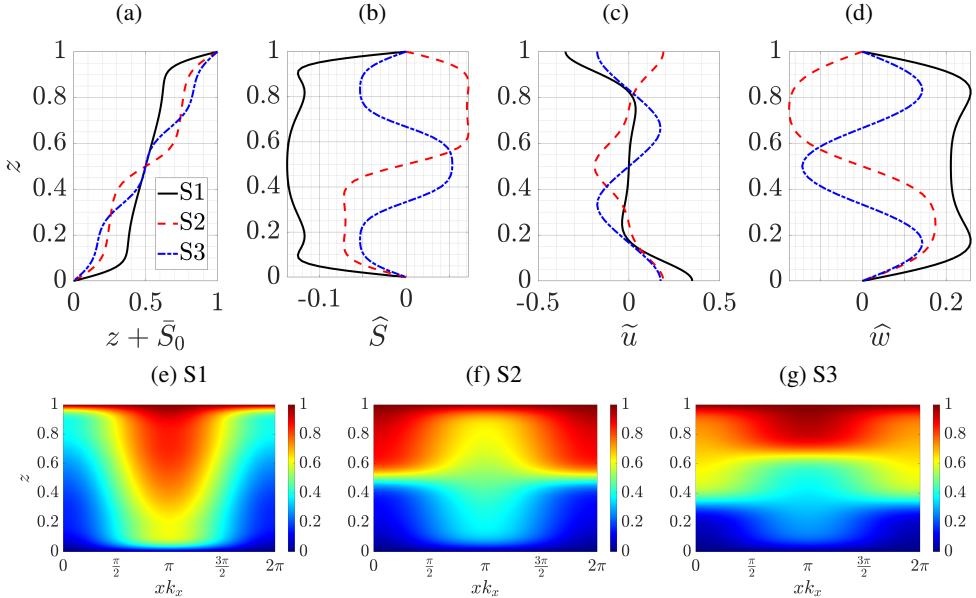


Figure 11: Solution profiles from the single-mode equations (2.7) in the same parameter regime as figure 3 but with stress-free velocity boundary conditions at top and bottom. The first row shows the profiles of (a) $z + \bar{S}_0$, (b) \hat{S} , (c) \tilde{u} , and (d) \hat{w} . The second row shows the reconstructed total salinity using (2.6a) and (2.1) for (e) S1, (f) S2, and (g) S3 solutions.

The A2 solution exhibits a similar profile as in the no-slip boundary condition case shown in figure 5(a), while the horizontally averaged salinity in A3 differs from that found with the no-slip boundary conditions. Figure 12(b) shows the isocontours of the streamfunction in A3, and shows two large and one small recirculation cell in the vertical direction, while figure 5(f) shows one large and two small cells in the vertical. Here, the A3 solution in the stress-free boundary condition case originates from a secondary bifurcation at $k_x = 13.665$ on the S3 branch, while there is another secondary bifurcation at $k_x = 13.703$ (not shown in figure 10) that is closer to the high wavenumber onset of the S3 state ($k_x = 15.573$) and that preserves midplane reflection symmetry. The mean salinity of the state shown in figure 12(c) resembles the mean temperature profile in magnetoconvection (Julien *et al.* 2000, figure

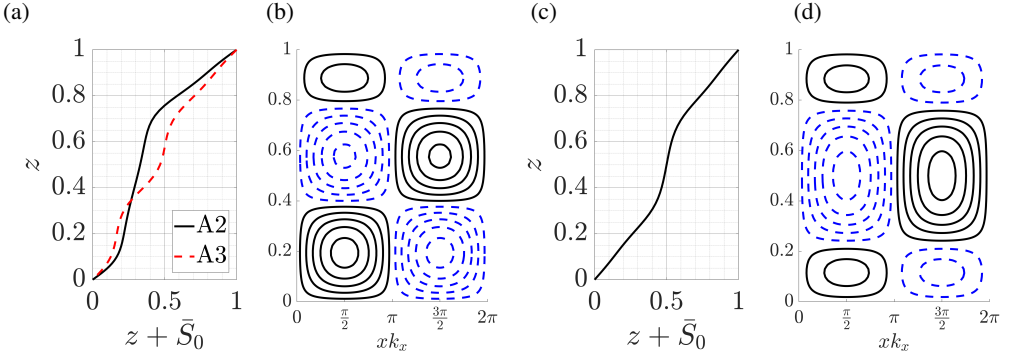


Figure 12: Solution profiles on the secondary branches computed from the single-mode equations (2.7) in the same parameter regime as figure 5 but with stress-free velocity boundary conditions at the top and bottom. Panel (a) shows the profiles of $z + \bar{S}_0$ of the A2 and A3 solutions, while panel (b) displays the isocontours of the streamfunction of the A3 solution. Panels (c) and (d) show $z + \bar{S}_0$ and the isocontours of the streamfunction for a steady solution preserving midplane reflection symmetry generated in a secondary bifurcation of the S3 solution.

7(b)), and the isocontours of the streamfunction in figure 12(d) show one large and two small closed streamlines that are similar to those in the A3 solution with no-slip boundary conditions in figure 5(f). The fact that this additional secondary bifurcation appears closer to the high wavenumber onset of S3 than the bifurcation to the A3 branch likely contributes to the difference in the solution profiles of the A3 state with stress-free and no-slip boundary conditions.

3.3. Dependence on density ratio

Oceanographic conditions display a wide range of density ratios, and this subsection therefore explores the dependence of our results on the density ratio. In particular, the staircases observed in oceanographic observations, laboratory measurements, and DNS are typically associated with the parameter regime $R_\rho \sim O(1)$ (Schmitt *et al.* 1987; Krishnamurti 2003, 2009; Radko 2003) that is far away from the onset of the salt-finger instability $R_{\rho,\text{crit}} = 1/\tau$ with $\tau = 0.01$.

Figure 13 shows the bifurcation diagram with density ratio $R_\rho = 2$ and no-slip boundary conditions for (a) 2D results with $k_y = 0$ and (b) 3D results with $k_y = k_x$. Here, we focus on the S1, S2, S3, TF1 solution branches, as well as a new traveling wave (TW1) solution branch that does not exist when $R_\rho = 40$. Here, the Sh of the S1, S2, and S3 solutions in the 2D and 3D configurations are still the same after converting the results by rescaling the horizontal wavenumber according to (3.3). However, the stability of the S1 solutions is now different and the secondary bifurcation points of S1 that lead to TF1 and TW1 also differ. This can be seen in the zoom of regions close to the appearance of TF1 and TW1 in figures 13(c)-(f). Specifically, the bifurcation points leading to the TF1 and TW1 branches in 2D are closer to the high wavenumber onset of the S1 solution than in 3D, suggesting that the 2D configuration forms tilted fingers or traveling wave solutions more readily. This is consistent with the suggestion that large-scale shear is generated more easily in a 2D configuration than in 3D (Goluskin *et al.* 2014).

The S1, S2 and S3 solution branches at $R_\rho = 2$ in figure 13 exhibit much larger Sh than those at $R_\rho = 40$ in figure 2. This is expected as a lower density ratio indicates stronger destabilization by the salinity gradient. Figure 14 shows profiles of the S1, S2 and S3 solutions at $R_\rho = 2$ and $k_x = 17.5$, $k_y = 0$. Here, the well-mixed region in the horizontally averaged

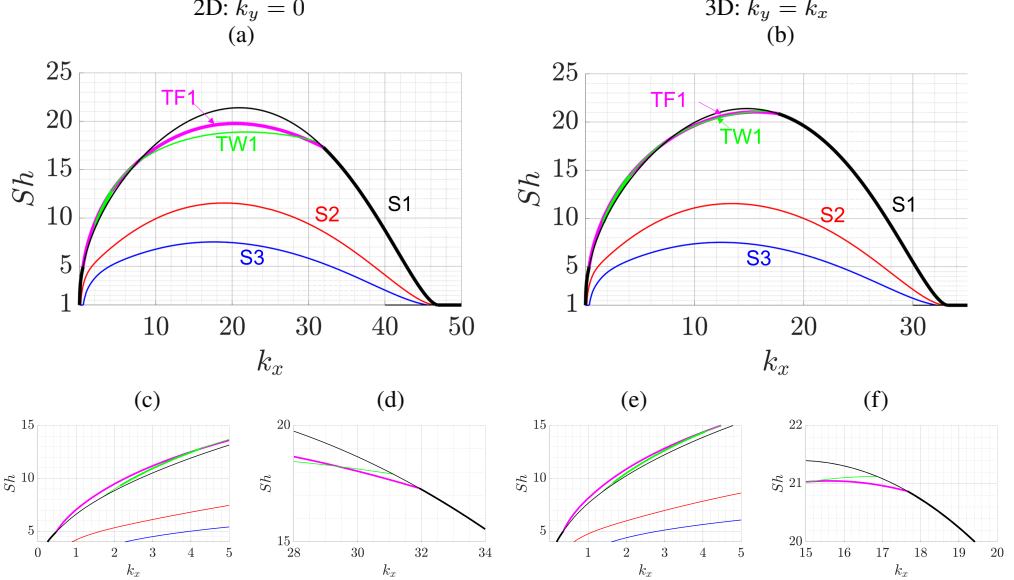


Figure 13: Bifurcation diagrams as a function of the wavenumber k_x from the single-mode equations (2.7) with (a) 2D: $k_y = 0$ and (b) 3D: $k_y = k_x$. The governing parameters are $R_\rho = 2$, $Pr = 7$, $\tau = 0.01$, and $Ra_T = 10^5$. Panels (c)-(d) are a zoom of the 2D results in panel (a) and panels (e)-(f) are a zoom of the 3D results in panel (b).

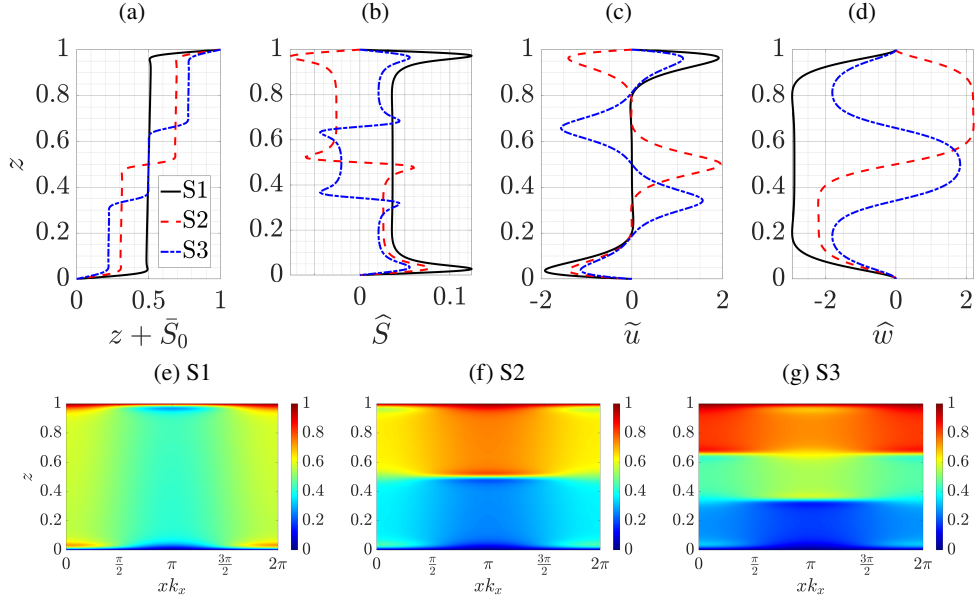


Figure 14: Solution profiles from the single-mode equations (2.7). The first row shows the profiles of (a) $z + \bar{S}_0$, (b) \hat{S} , (c) \tilde{u} and (d) \hat{w} . The second row shows the reconstructed total salinity using (2.6a) and (2.1) for (e) S1, (f) S2 and (g) S3 solutions. The parameter values are $k_x = 17.5$, $k_y = 0$, $R_\rho = 2$, $Pr = 7$, $\tau = 0.01$ and $Ra_T = 10^5$.

total salinity $z + \bar{S}_0(z)$ corresponds to almost constant salinity compared with the solution profile at $R_\rho = 40$ in figure 3. Outside of the well-mixed region, the profile $z + \bar{S}_0(z)$ at $R_\rho = 2$ exhibits a sharper interface compared with that at $R_\rho = 40$ in figure 3. This is consistent with the observation of well-defined staircases in flow regimes with $R_\rho \sim O(1)$ in field measurements (Schmitt *et al.* 1987) and laboratory experiments (Krishnamurti 2003, 2009) as well as in DNS (Radko 2003). The vertical profiles of the salinity harmonic \hat{S} in the S1, S2 and S3 states shown in figure 14(b) all show a local peak at the region associated with sharp interfaces. Both the horizontal velocity and the vertical velocity in figures 14(c)-(d) show a larger magnitude compared with the $R_\rho = 40$ results in figures 3(c)-(d).

We now focus on the solutions TF1 and TW1 originating from secondary bifurcations of the S1 state. Figure 15(a) shows the associated large-scale shear $\bar{U}_0(z)$ of TF1 and TW1. This shear is antisymmetric with respect to the midplane for TF1 but symmetric for TW1. Figure 15(b) shows the total salinity profile for a tilted finger with a larger tilt angle compared with the tilt at $R_\rho = 40$ shown in figure 4(e). Figure 14(c) shows the total salinity of TW1 in the comoving frame, with structures that tilt in opposite directions above and below the midplane. This alternating tilt direction resembles the ‘wavy fingers’ tilted either left or right observed in experiments (Krishnamurti 2003, figure 7), although whether such ‘wavy fingers’ travel depends on the boundary conditions in the horizontal.

The stability properties of these solutions are also indicated in figure 13 and are similar to those for high density ratios (figure 2). Here, the S1 solution is stable near the onset, but loses stability to tilted fingers. The solutions S2 and S3 are still unstable within all of the current parameter regime. The traveling wave appears to gain stability within a certain wavenumber regime close to the low wavenumber onset, as indicated in the zoom in figures 13(c) and 13(e). Since the single-mode solutions are expected to be more accurate in the high wavenumber regime, cf. figure 2(a), we postpone a study of the dynamics of TF1 and TW1 to the lower Prandtl number considered in §4 where these states form at higher wavenumbers.

Figure 16 displays the dependence of the Sh on the density ratio R_ρ for $\tau = 0.01$ for 3D results with $k_y = k_x$ based on the scaling law

$$k_x = k_y = R_\rho^{0.125} \pi / (14.8211 Ra_S^{-0.2428}), \quad (3.6a)$$

$$Ra_S := \frac{g\beta \Delta Sh^3}{\kappa_S \nu} = \frac{Ra_T}{R_\rho \tau}, \quad (3.6b)$$

obtained through a least-squares fit of the finger width computed from 3D DNS (Yang *et al.* 2016a, figure 13(b)). Here, we can see that the S1 solution remains stable near onset, and then bifurcates to stable tilted fingers (TF1) as R_ρ decreases. The figure also shows the Sh from 3D DNS data (Yang *et al.* 2015, table 1) using black stars. We also perform 2D direct numerical simulations in domains of size $L_x = 2\pi/k_{x,2D} = 2\pi/(\sqrt{2}k_x)$ with k_x given by (3.6a). Note that our simulation results do not display a smooth transition to the Sh from the 3D results (Yang *et al.* 2015), which is likely due to the intrinsic difference between 2D and 3D simulations and possibly different domain sizes. However, the Sh obtained from the S1 single-mode solutions agree well with the DNS results near the high density ratio onset. At lower density ratios, the single-mode solution S1 and TF1 both overpredict the DNS results. This may be because both are steady-state solutions, while the DNS results exhibit time-dependent behavior which likely reduces the time-averaged Sh number.

We find that $Sh \sim R_\rho^{-0.30}$ for the single-mode solutions within the range $R_\rho \in [0.1, 2]$ indicating that $Sh \sim Ra_S^{0.30}$ as a function of the salinity Rayleigh number defined in (3.6b) and fixed Ra_T and τ . This result agrees well the scaling law of Nusselt number $Nu \sim Ra_T^{0.30} (\ln Ra_T)^{0.20}$ obtained from single-mode solutions for Rayleigh-Bénard convection and wavenumber scaling as $k_x \sim Ra_T^{1/4}$ (Gough *et al.* 1975, p. 713). Figure 16(b) displays

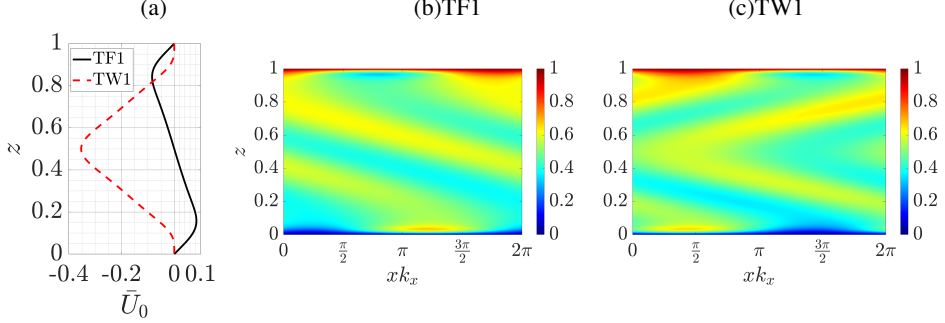


Figure 15: Solution profiles of (a) TF1 and (b) TW1 from the single-mode equations (2.7) showing the associated large-scale shear \bar{U}_0 and the isocontours of total salinity. The governing parameters are $k_x = 17.5$, $k_y = 0$, $R_\rho = 2$, $Pr = 7$, $\tau = 0.01$ and $Ra_T = 10^5$.

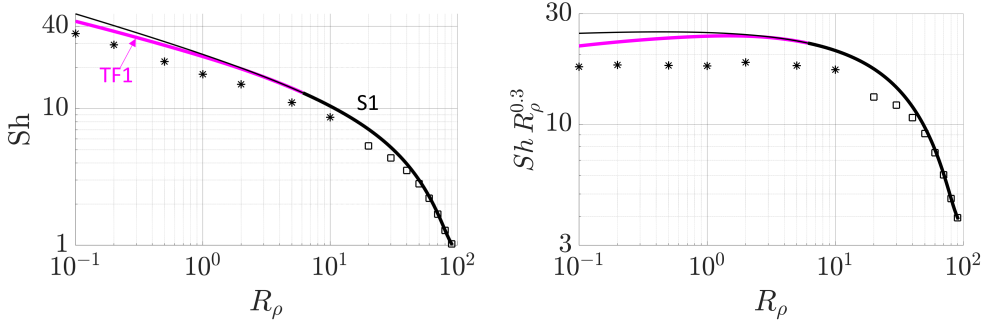


Figure 16: (a) Bifurcation diagrams displaying Sh as a function of the density ratio R_ρ from the single-mode equations (2.7) with wavenumbers k_x and k_y given by the scaling law (3.6a). The other parameters are $Pr = 7$, $\tau = 0.01$ and $Ra_T = 10^5$. The black star (*) is obtained from 3D DNS (Yang *et al.* 2015, table 1). The black square (□) is obtained from 2D DNS results in a horizontal domain of size $L_x = 2\pi/k_{x,2D} = 2\pi/(\sqrt{2}k_x)$ with k_x given by (3.6a). Panel (b) plots the results in (a) in compensated form to exhibit the scaling exponent.

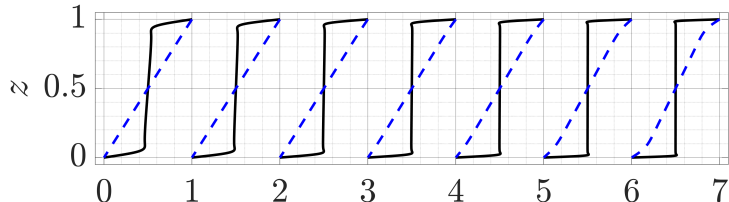


Figure 17: Solution profiles from the single-mode equations (2.7) displaying horizontally averaged total salinity (black solid lines) and horizontally averaged total temperature (blue dashed lines). Solution profiles are labeled by integers and correspond to $R_\rho = 10, 5, 2, 1, 0.5, 0.2$, and 0.1 from left to right. Other parameter values are $Pr = 7$, $\tau = 0.01$, $Ra_T = 10^5$, with $k_x = k_y$ given by the scaling law in (3.6a).

the compensated Sherwood number $Sh R_\rho^{0.30}$, showing that the S1 solutions from both the single-mode approach and DNS (Yang *et al.* 2015) follow the same $Sh \sim R_\rho^{-0.3}$ scaling law. Note that the DNS results for salt-finger convection in the asymptotic regime of high Ra_S instead suggest $Sh \sim Ra_S^{1/3}$ (Yang *et al.* 2015, figure 7(a)) while experimental results

suggest $Sh \sim Ra_S^{4/9}$ (Hage & Tilgner 2010, figure 8). The parameter regime considered here is within the regime $Ra_S \leq 10^8$, a value that may be insufficient to reliably establish the asymptotic scaling; see e.g., (Yang *et al.* 2015, figure 7(a)) and (Yang *et al.* 2016b, figure 3(a)). The TF1 solutions suggest the scaling law $Sh \sim R_\rho^{-0.27}$ or $Sh \sim Ra_S^{0.27}$ for fixed Ra_T and τ . This is consistent with the observation in Rayleigh-Bénard convection that the formation of the large-scale shear decreases the scaling exponent η of $Nu \sim Ra_T^\eta$; see e.g., Goluskin *et al.* (2014, figure 4).

Figure 17 shows the corresponding mean salinity and temperature profiles at the same parameter values as those used for the 3D DNS results in Yang *et al.* (2015, figure 2(a)). The solution profiles from the single-mode equations closely match the qualitative trend of the mean salinity and temperature profiles as a function of the density ratio in the DNS results (Yang *et al.* 2015, figure 2(a)). In particular, both the single-mode and DNS results show that the mean salinity profile displays a well-mixed region in the layer interior, and that both show a small overshoot (a thin stably stratified region) near the top and bottom boundaries. The mean total temperature remains close to a linear profile, however, and shows a visible deviation from a linear profile only at $R_\rho = 0.1$, a fact also consistent with DNS observation (Yang *et al.* 2015, figure 2(a)).

4. Tilted salt fingers and traveling waves at $Pr = 0.05$

The bifurcation diagram for a low density ratio, $R_\rho = 2$, and $Pr = 7$ displays a branch of steady tilted fingers (TF1) and a branch of traveling waves (TW1), both of which bifurcate from the symmetric one-layer solution S1 at intermediate wavenumbers. Here, we study these states in the low Prandtl number regime that pushes the bifurcations to TF1 and TW1 to higher wavenumbers and hence closer to the high wavenumber onset, where we expect the single-mode solutions to be accurate. Low Prandtl number salt-finger convection is of interest in astrophysical applications, where molecular weight gradients compete with thermal buoyancy but heat transport is dominated by photon diffusion (Garaud 2018). However, to keep the notation consistent with the previous sections, we continue to use the symbol S to represent the higher molecular weight component and refer to it as salinity.

Figure 18 shows the bifurcation diagram for the parameter values used in figure 2 but with $Pr = 0.05$. Here, we focus on the solution branches S1, TF1 and TW1. Compared with the $Pr = 7$ results in figure 2, we see that the Sh associated with the S1 solution remains the same, but the bifurcation to TF1 ($k_x = 17.593$) now occurs much closer to the high wavenumber onset of the S1 solution ($k_x = 19.251$). Moreover, the traveling wave branch TW1 that is present here does not appear at $R_\rho = 40$, $Pr = 7$ in figure 2. Evidently low Prandtl numbers favor spontaneous formation of large-scale shear, as found in DNS by Radko (2010, figures 1-2) and Garaud & Brummell (2015) as well as in a reduced model valid in the asymptotic limit of low τ and low Pr (Xie *et al.* 2019).

A comparison between 2D and 3D results at $Pr = 0.05$ in figure 18 shows that the bifurcation point of TF1 and TW1 is closer to the high wavenumber onset of S1 in the 2D configuration. The difference between 2D and 3D at $Pr = 0.05$ in figure 18 is more evident than that at $Pr = 7$ in figure 2, as is the case in Rayleigh-Bénard convection (van der Poel *et al.* 2013). Recalling that both TF1 and TW1 are associated with the formation of large-scale shear (see table 2, and figures 15(a) and 19(b)), this difference suggests that the 2D configuration favors the formation of large-scale shear, cf. (Garaud & Brummell 2015).

Figure 19 shows the solution profiles in the TF1 and TW1 states. Here we choose a 3D wavenumber $k_y = k_x = 6.873$ close to the wavenumber that maximizes the Sh in the S1 solution. Similar to the earlier observation of tilted fingers in figure 4, the mean total salinity profile $z + \bar{S}_0(z)$ of TF1 shows two relatively well-mixed regions with a linear profile in the

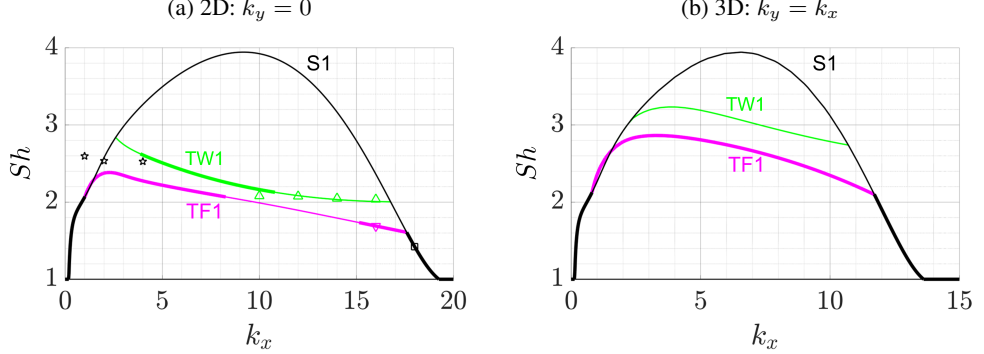


Figure 18: Bifurcation diagrams as a function of the wavenumber k_x from the single-mode equations (2.7) for (a) 2D: $k_y = 0$ and (b) 3D: $k_y = k_x$. Other parameters are $\bar{R}_\rho = 40$, $Pr = 0.05$, $\tau = 0.01$, and $Ra_T = 10^5$. The markers correspond to the Sh associated with steady states resembling S1 (□), TF1 (▽) and TW1 (△) solutions from 2D DNS in domains of size $L_x = 2\pi/k_x$ (table 4). The black pentagrams corresponding to the Sh at $L_x = 2\pi/k_x$ ($k_x = 1, 2, 4$) indicate chaotic behavior.

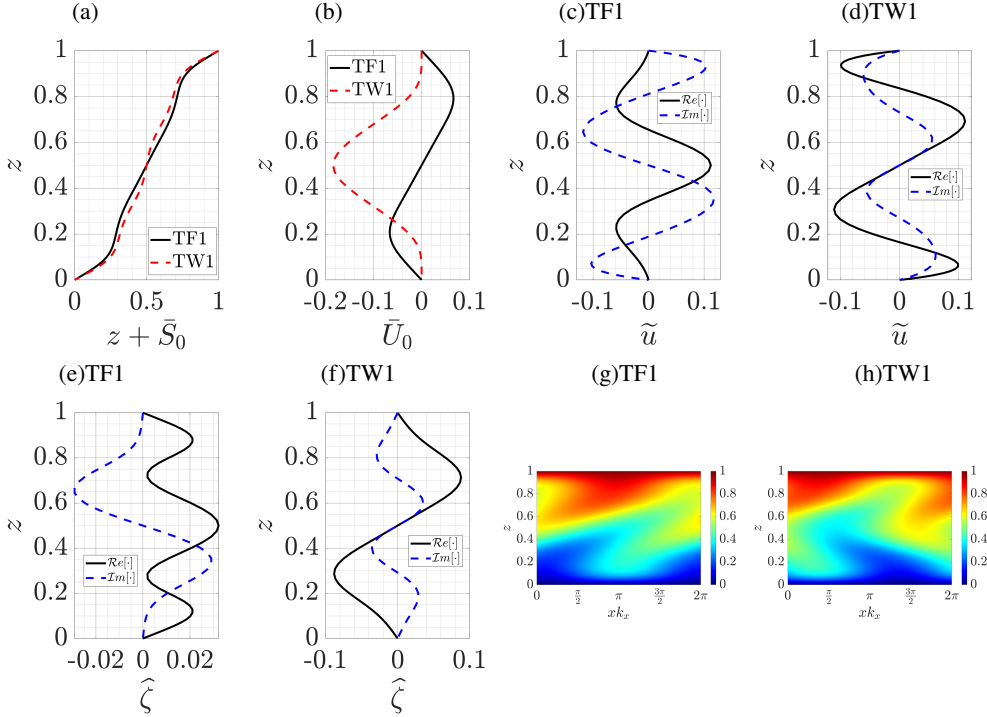


Figure 19: Solution profiles from the single-mode equations (2.7) for the TF1 and TW1 solutions displaying (a) $z + \bar{S}_0$, (b) \bar{U}_0 and the horizontal velocity \tilde{u} for (c) TF1 and (d) TW1. The second row shows the vertical vorticity mode for (e) TF1 and (f) TW1 and the isocontours of the total salinity for (g) TF1 and (h) TW1 using (2.6a) and (2.1). Other parameter values are $k_x = k_y = 6.873$, $R_\rho = 40$, $Pr = 0.05$, $\tau = 0.01$ and $Ra_T = 10^5$.

		L_x	2π/18	2π/16	2π/14	2π/12	2π/10	2π/8	2π/6	2π/4	2π/2	2π	4π
I.C.													
S1	S1	S1	TF1	RTF	RTF	RTF	C	RTF (2)	C	C	C	C	C
TF1	-	-	TF1	RTF	RTF	RTF	C	RTF (2)	C	C	-	-	-
TW1	-	-	TF1	RTF	RTF	RTF	C	RTF (2)	C	-	-	-	-

Table 4: The flow structures from 2D DNS at $t = 3000$ in domains of different sizes L_x and initial conditions (I.C.) constructed from the single-mode approximations to the S1, TF1 and TW1 states using the ansatz (2.6) with $k_x = 2\pi/L_x$, $k_y = 0$. RTF indicates direction-reversing tilted fingers and C represents chaotic behavior; ‘-’ indicates that a nonzero single-mode solution at $k_x = 2\pi/L_x$ is not present based on figure 18(a). The number $n \in \mathbb{Z}$ inside a bracket indicates the horizontal wavenumber $k_x = 2\pi n/L_x$ reached at $t = 3000$ if different from the initial wavenumber $n = 1$.

middle of the layer. In contrast, the TW1 shows instead a three-layer structure in $z + \bar{S}_0(z)$. Panel (b) in figure 19 displays the associated large-scale shear $\bar{U}_0(z)$, and exhibits a similar structure to that observed at $R_\rho = 2$, $Pr = 7$ in figure 15(a). Figures 19(c)-(d) display the vertical profile of the first harmonic of the horizontal velocity \tilde{u} in the TF1 and TW1 states showing local peaks close to $z = 1/3$, $1/2$, and $2/3$, in contrast to the corresponding S1 solution that displays peaks near the boundaries. These properties are in turn reflected in the staircase profile of the mean salinity shown in figure 19(a).

Furthermore, in 3D the TF1 and TW1 solutions are also associated with nonzero vertical vorticity as shown in figures 19(e)-(f). Here, the generation of the vertical vorticity originates from the large-scale horizontal shear \bar{U}_0 , which provides a source term for the vertical vorticity equation (2.7b). Vertical vorticity is also generated in bifurcations of steady convection rolls (resembling S1) in single-mode solutions of Rayleigh-Bénard convection on a hexagonal lattice (Lopez & Murphy 1983; Murphy & Lopez 1984; Massaguer & Mercader 1988; Massaguer *et al.* 1990) with a source term provided by self-interaction on this lattice (e.g. Massaguer *et al.* (1990, equation (2.2b))). As the current single-mode formulation is limited to roll or square planforms, this source term is not present. Instead, it is the associated large-scale shear \bar{U}_0 that provides the source term for vertical vorticity, a possibility not included in the previous work (Lopez & Murphy 1983; Murphy & Lopez 1984; Massaguer & Mercader 1988; Massaguer *et al.* 1990).

The salinity profiles of TF1 and TW1 are shown in figures 19(g)-(h). These panels show qualitative similarity with the TF1 and TW1 shown in figures 15(b)-(c), where the TF1 solution is tilted in one direction, while the TW1 is tilted in opposite directions above and below the midplane. However, the TF1 and TW1 at $R_\rho = 2$, $Pr = 7$ in figure 15 show a relatively well-mixed region in the interior, $z \approx 1/2$, compared with the TF1 and TW1 at the higher density ratio $R_\rho = 40$ but small Prandtl number, $Pr = 0.05$, shown in figure 19.

The stability of these solutions is indicated in figure 18 by thick (stable) and thin (unstable) lines. In 2D TF1 is stable near the onset of this branch, but becomes unstable at an intermediate wavenumber. The traveling wave is instead unstable near the onset, but then gains stability over an interval of intermediate wavenumbers before losing it again, cf. the TW1 branch at $R_\rho = 2$ and $Pr = 7$ in figure 13. In 3D the TF1 branch is always stable, as in the high Prandtl number regime, cf. figures 2 and 13, while the TW1 branch is always unstable, cf. figure 18(b).

We next compare these results with those from 2D DNS following our analysis of the $Pr = 7$ results in table 3. The domain length L_x in the horizontal is taken from $[2\pi/18, 4\pi]$ and the initial conditions are, respectively, constructed using the S1, TF1, and TW1 single-mode solutions with $k_x = 2\pi/L_x$ and $k_y = 0$. In this L_x interval single-mode theory predicts that S1, TF1 or TW1 may be stable. In table 4 we record the state reached in each case at $t = 3000$. We find that the DNS returns S1 or TF1 depending on initial conditions but also supports direction-reversing tilted fingers (RTF) and chaotic states (C). In particular, with horizontal domain $L_x = 2\pi/18$, the final state exhibits S1 behavior consistent with the single-mode prediction and the Sh from DNS overlaps with the prediction from single-mode equations as shown in figure 18(a). For $L_x = 2\pi/16$, the final state in table 4 shows TF1, which is the only stable solution in single-mode theory at $k_x = 16$. The corresponding Sh at $L_x = 2\pi/16$ from DNS also overlaps with the TF1 single-mode solution as shown in figure 18(a).

In order to demonstrate the fidelity of the single-mode TW1 solutions near the high wavenumber onset, figure 20 compares one DNS run with $L_x = 2\pi/14$ and a TW1 single-mode initial condition. The solution takes the form of a traveling wave up to $t \approx 400$, and consequently we compare the time average of this state over $t \in [100, 300]$ with the corresponding single-mode results. Specifically, figure 20(a) shows the horizontally averaged horizontal velocity $\langle u \rangle_h(z, t)$ corresponding to the large-scale shear mode $\bar{U}_0(z, t)$ in the single-mode equations. Figures 20(b)-(c) demonstrate an essentially perfect agreement between the $z + \langle S \rangle_{h,t}$ and $\langle u \rangle_{h,t}$ profiles computed from the DNS in this time interval and their counterparts $z + \bar{S}_0$ and \bar{U}_0 computed from the TW1 branch of the single-mode solutions at $k_x = 2\pi/L_x = 14$ and the same parameters. The Sh also agrees with the single-mode prediction as indicated in figure 18(a). At $t \approx 400$, the TW1 state undergoes an abrupt transition to an oscillatory state with an antisymmetric mean shear profile suggesting that this state is a tilted finger state whose tilt direction reverses periodically in time, i.e., it is direction-reversing tilted finger (RTF). Similar behavior was also found at $Pr = 7$ with $L_x = 2\pi/8$ initialized by an S2 solution; see table 3 and figure 6. All RTF states in tables 3 and 4 were identified based on the direction-reversing behavior of the associated large-scale shear $\langle u \rangle_h(z, t)$.

Direction-reversing tilted fingers are also observed as the final state in larger horizontal domains with $L_x = 2\pi/12$, $2\pi/10$ and $2\pi/6$ as shown in table 4. Figure 21 shows the DNS results with $L_x = 2\pi/10$ and initial condition S1. The total salinity $z + S$ at the midplane $z = 1/2$ in figure 21(a) shows that the initial state is sinusoidal in space and steady, corresponding to the prescribed S1 solution. After $t \approx 80$, the S1 state transitions into a traveling wave and subsequently, at $t \approx 220$, into an RTF state. Figure 21(b) shows that $\langle u \rangle_h(z, t) = 0$ at $t = 0$ but then this quantity becomes nonzero and midplane-symmetric at the transition to the TW state with superposed periodic oscillations. Figures 21(c)-(d) present the horizontally averaged total salinity profiles, respectively averaged over $t \in [80, 180]$ and $t \in [280, 380]$, corresponding to the traveling wave and the direction-reversing tilted fingers, and compared with $z + \bar{S}_0$ for the single-mode TW1 and TF1 solutions with $k_x = 2\pi/L_x$ and the same parameter values. Here, both the DNS results and the single-mode solutions show a modest three-layer staircase characteristic of the traveling wave state, while both show a two-layer staircase with a linear profile in the middle that is associated with direction-reversing tilted fingers in DNS and the tilted finger state of the single-mode equations.

Figure 21(e) shows $\langle u \rangle_{h,t}$ from the DNS averaged over $t \in [80, 180]$ corresponding to the traveling wave, and compares it with \bar{U}_0 from the corresponding single-mode TW1 solution. Here, the large-scale shear from the single-mode theory overpredicts the amplitude compared to that observed in DNS. This is expected as figure 21(b) indicates that the state is in fact a

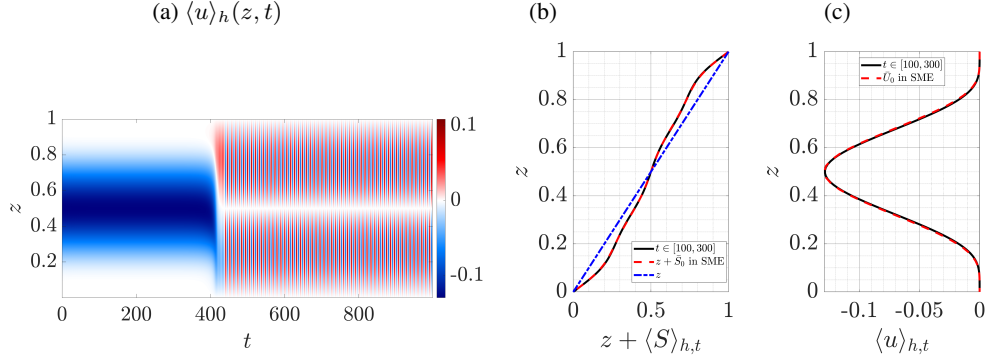


Figure 20: 2D DNS of a traveling wave showing (a) $\langle u \rangle_h(z, t)$, (b) $z + \langle S \rangle_{h,t}(z)$ and (c) $\langle u \rangle_{h,t}(z)$ averaged over $t \in [100, 300]$ (black lines) for comparison with $z + \bar{S}_0$ and \bar{U}_0 from the single-mode TW1 branch (red dashed lines). The parameters are $R_\rho = 40$, $Pr = 0.05$, $\tau = 0.01$, and $Ra_T = 10^5$. The initial condition is a TW1 solution with $L_x = 2\pi/14$ for the DNS; the single-mode solutions are computed for $k_x = 2\pi/L_x = 14$, $k_y = 0$.

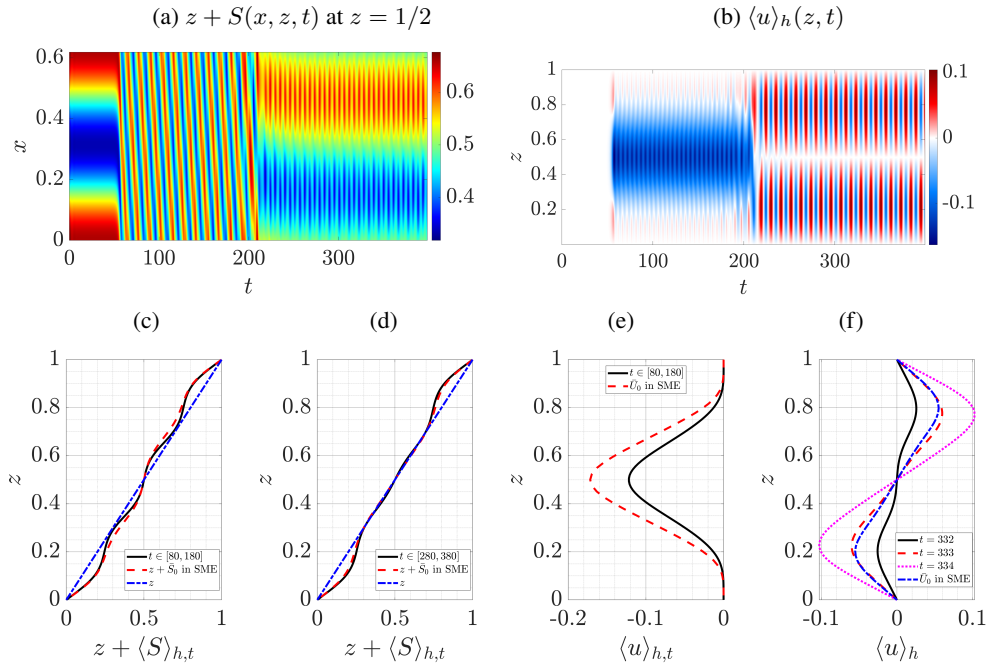


Figure 21: 2D DNS showing space-time plots of (a) $z + S(x, z, t)$ at $z = 1/2$ and (b) $\langle u \rangle_h(z, t)$. Panels (c) and (d) show the profiles of $z + \langle S \rangle_{h,t}(z)$ averaged over $t \in [80, 180]$ for the traveling wave episode, and $t \in [280, 380]$ for direction-reversing tilted fingers, and compared with $z + \bar{S}_0$ from the single-mode TW1 and TF1 solutions. Panel (e) shows $\langle u \rangle_{h,t}$ averaged over $t \in [80, 180]$ and compared with \bar{U}_0 for the single-mode TW1 branch, while (f) shows $\langle u \rangle_h(z, t)$ at $t = 332, 333$ and 334 for comparison with \bar{U}_0 from the single-mode TF1 solution. The initial condition is a S1 solution with $L_x = 2\pi/10$, and other parameters are $R_\rho = 40$, $Pr = 0.05$, $\tau = 0.01$, $Ra_T = 10^5$. The single-mode solutions are calculated for $k_x = 2\pi/L_x = 10$, $k_y = 0$. See supplementary video 3.

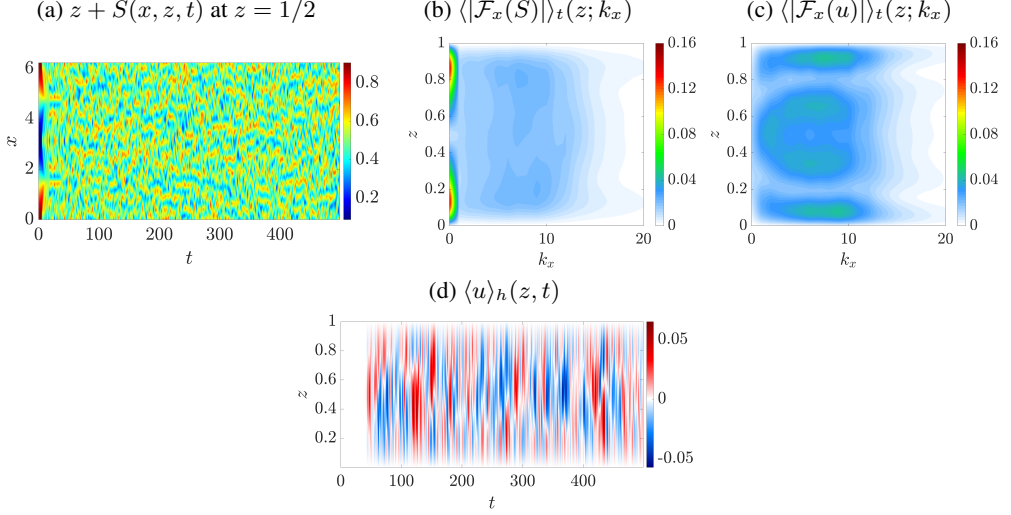


Figure 22: 2D DNS results showing (a) total salinity at $z = 1/2$, (b) $\langle |F_x(S)| \rangle_t(z; k_x)$, (c) $\langle |F_x(u)| \rangle_t(z; k_x)$ and (d) $\langle u \rangle_h(z, t)$. The horizontal domain size is $L_x = 2\pi$ initialized by the corresponding S1 solution. The parameters are $R_\rho = 40$, $Pr = 0.05$, $\tau = 0.01$, and $Ra_T = 10^5$.

modulated traveling wave with superposed oscillations in $\langle u \rangle_h$ in $t \in [80, 180]$. Moreover, as shown previously in figures 2(a) and 18(a), the accuracy of the single-mode equation is expected to decrease with decreasing wavenumber (here $k_x = 10$), a fact that may account for the difference in the solution profiles between DNS and single-mode theory. This difference in the large-scale shear may also contribute to the difference in the mean salinity profiles in figure 21(c) and the associated Sh in figure 18(a). As the TF1 solution in the single-mode equation is steady, we compare the large-scale shear \bar{U}_0 with three different snapshots of $\langle u \rangle_h(z, t)$ at $t = 332, 333, 334$ in figure 21(f). The shape and magnitude of $\langle u \rangle_h$ at $t = 333$ is close to a TF1 single-mode solution, but the maximum amplitude of the large-scale shear of RTF observed in 2D DNS is larger than \bar{U}_0 from the TF1 single-mode solution.

For larger L_x , the solution may transition to a double wavenumber RTF, see $L_x = 2\pi/6$ in table 4, and such a transition to a higher wavenumber flow structure was already described for $Pr = 7$ as summarized in table 3 and figures 7 and 8. Since the final state does not exhibit well-organized flow structures when $L_x \in [2\pi/4, 4\pi]$ we refer to it as chaotic. Figure 22 presents (a) the total salinity at the midplane, (b) the Fourier-transformed salinity deviation $\langle |F_x(S)| \rangle_t$, and (c) the Fourier-transformed horizontal velocity $\langle |F_x(u)| \rangle_t$. Here, we select $L_x = 2\pi$ and the initial condition is a S1 solution, so the only difference between the results in figures 22 and 9 is the value of the Prandtl number. The total salinity at the midplane $z = 1/2$ in figure 22(a) at $Pr = 0.05$ does not show a very clear difference from figure 9(a) at $Pr = 7$, while the Fourier spectrum of the salinity at $P = 0.05$ in figure 22(b) is broader than the same quantity at $Pr = 7$ in figure 9(b). The Fourier-transformed horizontal velocity in figure 22(c) shows a greater difference from the corresponding result at $Pr = 7$ in figure 9(c), where the peaks near $z = 1/3$ and $z = 2/3$ and the peak at $z = 1/2$ at $k_x \approx 1$ have magnitudes similar to those near the boundary. This suggests that both TF1 and TW1 are involved in the chaotic behavior. Moreover, $\langle |F_x(u)| \rangle_t$ shows a nonzero value at $k_x = 0$ corresponding to the large-scale shear in figure 22(c), while the white region in $\langle |F_x(u)| \rangle_t$ at $k_x = 0$ in figure 9(c) for $Pr = 7$ indicates a value close to zero. This is consistent with the fact that low Prandtl numbers favor the formation of large-scale shear. Indeed, $\langle u \rangle_h(z, t)$ in

figure 22(d) reaches a maximum value of 0.065, while the same quantity has the maximum amplitude 5.37×10^{-4} when $Pr = 7$.

At other times, the large-scale shear $\langle u \rangle_h(z, t)$ in figure 22(d) resembles the large-scale shear $\bar{U}(z)$ associated with either TF1 or TW1 in figure 19(b) based on the parity of $\langle u \rangle_h(z, t)$ with respect to $z = 1/2$. The observed time series suggests that the solution visits the neighborhoods of both the traveling waves and the tilted fingers in a chaotic manner. The mean Sh associated with this state in domains of size $L_x = \pi/2, \pi$ and 2π , and initialized using the S1 single-mode solution are shown in figure 18(a), and fall within the range predicted by S1, TF1, and TW1 single-mode states. Note that for these relatively large domain sizes, transition to a higher wavenumber mode is also possible but cannot be predicted within the single-mode approach. The comparison in figure 18(a) supports the role of the (unstable) TF1 and TW1 solutions in determining the salinity transport in this chaotic state.

5. Conclusions and future work

This work performed bifurcation analysis of vertically confined salt-finger convection using single-mode equations obtained from a severely truncated Fourier expansion in the horizontal. The resulting equations were solved for the vertical structure of the solutions as a function of the density ratio, the Prandtl number, and the assumed horizontal wavenumber. We fixed the diffusivity ratio and thermal Rayleigh number and focused almost exclusively on the case of no-slip velocity boundary conditions. We computed strongly nonlinear staircase-like solutions having one (S1), two (S2) and three (S3) well-mixed mean salinity regions in the vertical direction. These bifurcate in successive bifurcations from the trivial solution. In each case, salinity gradients are expelled from regions of closed streamlines resembling the mechanism described by Rhines & Young (1983), leading to a well-mixed interior. Secondary bifurcations of S1 lead to tilted fingers (TF1) or traveling waves (TW1) both of which spontaneously break reflection symmetry in the horizontal owing to the spontaneous generation of large-scale shear. Secondary bifurcations from S2 and S3 lead to asymmetric solutions (A2 and A3) that spontaneously break symmetry with respect to the horizontal midplane.

The stability and relevance of the single-mode solutions we obtained were further analyzed with the assistance of 2D DNS. Near onset, the one-layer solution S1 is stable and corresponds to maximum salinity transport among the three solutions, an observation consistent with the prediction of ‘relative stability’ criterion (Malkus & Veronis 1958). The associated Sherwood number near the high wavenumber onset is in excellent agreement with DNS in small horizontal domains. In larger domains DNS reveals that the final state reverts to a higher wavenumber S1 state closer to the natural finger scale or exhibits chaotic behavior. In general the final state exhibits strong dependence on initial conditions. The S2, S3, A2 and A3 solutions are all unstable within the parameter regime explored, although the chaotic solutions we found appear to visit neighborhoods of these unstable solutions at different instants in time. With stress-free velocity boundary conditions the S1, S2, S3, TF1, A2 and A3 solutions persist whenever the density ratio and the Prandtl number are high enough, but exhibit larger Sherwood numbers.

At lower density ratios, the S1, S2 and S3 solutions exhibit sharper staircase structure, while the TF1 solution displays stronger large-scale shear and tilt angle. In addition S1 also bifurcates to the TW1 state, a bifurcation that is not present at high density ratio. The scaling of the S1 Sherwood number with the density ratio closely matches the DNS results within the currently explored parameter regime, while the corresponding change in the mean salinity and temperature profiles resembles that seen in DNS.

The dynamics of the secondary TF1 and TW1 states in the low Prandtl number regime also show excellent agreement with the 2D DNS results in small domains, likely because they appear, in this regime, quite close to the high wavenumber onset of S1. These states are typically associated with two- and three-layer mean salinity profiles, respectively. The final state seen in low Prandtl number 2D DNS is a prominent direction-reversing tilted finger (RTF) in which the tilt and the associated large-scale shear reverse periodically with time in a manner that resembles the ‘pulsating wave’ state identified in magnetoconvection (Matthews *et al.* 1993; Proctor *et al.* 1994). In smaller domains the time-averaged salinity and shear profiles computed from 2D DNS resemble the two-layer and three-layer mean salinity and shear profiles corresponding to RTF and TW1, respectively, while in larger domains such profiles are still evident but only episodically.

The bifurcation diagrams of single-mode solutions shown here also shed light on the difference between 2D and 3D. While the corresponding S1, S2, S3, A2 and A3 states in 3D can be obtained from the 2D results by a simple wavenumber rescaling, this is no longer so for states associated with large-scale shear, i.e. TF1 and TW1. The resulting difference is most prominent at low density ratio or low Prandtl numbers. A comparison shows that 2D favors the generation of large-scale shears, a fact consistent with DNS observations (Garaud & Brummell 2015).

The bifurcation diagram presented here is far from complete. Whether other primary or secondary bifurcations possess the potential to provide stable staircase solutions is an interesting question for future exploration. The secondary Hopf and global bifurcations are also of interest since they provide additional insight into the origin of the direction-reversing tilted finger state and of chaotic salt-finger convection, respectively. Extension of the present framework to 3D states with hexagonal coordination in the horizontal is also of interest, as is a study of the doubly- or triply-periodic configuration with periodic boundary conditions in the vertical as well as in the horizontal, a formulation that is likely to have greater relevance to oceanography. Finally, density staircases have also been widely observed in the diffusive regime of double-diffusive convection (cold fresh water on top of warm salty water) (Timmermans *et al.* 2008; Radko 2016; Yang *et al.* 2022) as well as in stratified shear flow (Oglethorpe *et al.* 2013; Taylor & Zhou 2017; Lucas *et al.* 2017, 2019) and elsewhere. It is of interest to explore the applicability of the present bifurcation-theoretic approach to the study of staircase states in these flow regimes.

Acknowledgment

This work was supported by the National Science Foundation under Grant Nos. OCE 2023541 (C.L. and E.K.) and OCE-2023499 (K.J.).

Declaration of Interests

The authors report no conflict of interest.

REFERENCES

- ASCHER, U. M., RUUTH, S. J. & SPITERI, R. J. 1997 Implicit-explicit Runge-Kutta methods for time-dependent partial differential equations. *Appl. Numer. Math.* **25**, 151–167.
- BAKER, L. & SPIEGEL, E. A. 1975 Modal analysis of convection in a rotating fluid. *J. Atmos. Sci.* **32**, 1909–1920.
- BALMFORTH, N. J., LLEWELLYN SMITH, S. G. & YOUNG, W. R. 1998 Dynamics of interfaces and layers in a stratified turbulent fluid. *J. Fluid Mech.* **355**, 329–358.

- BASSOM, A. P. & ZHANG, K. 1994 Strongly nonlinear convection cells in a rapidly rotating fluid layer. *Geophys. Astrophys. Fluid Dyn.* **76**, 223–238.
- BLENNERHASSETT, P. J. & BASSOM, A. P. 1994 Nonlinear high-wavenumber Bénard convection. *IMA J. Appl. Math.* **52**, 51–77.
- BURNS, K. J., VASIL, G. M., OISHI, J. S., LECOANET, D. & BROWN, B. P. 2020 Dedalus: A flexible framework for numerical simulations with spectral methods. *Phys. Rev. Res.* **2**, 023068.
- CALKINS, M. A., JULIEN, K., TOBIAS, S. M., AURNOU, J. M. & MARTI, P. 2016 Convection-driven kinematic dynamos at low Rossby and magnetic Prandtl numbers: single mode solutions. *Phys. Rev. E* **93**, 023115.
- CRAWFORD, J. D. & KNOBLOCH, E. 1991 Symmetry and symmetry-breaking bifurcations in fluid dynamics. *Annu. Rev. Fluid Mech.* **23**, 341–387.
- ELDER, J. W. 1969 The temporal development of a model of high Rayleigh number convection. *J. Fluid Mech.* **35**, 417–437.
- FER, I., NANDI, P., HOLBROOK, W. S., SCHMITT, R. W. & PÁRAMO, P. 2010 Seismic imaging of a thermohaline staircase in the western tropical North Atlantic. *Ocean Sci.* **6**, 621–631.
- GARAUD, P. 2018 Double-diffusive convection at low Prandtl number. *Annu. Rev. Fluid Mech.* **50**, 275–298.
- GARAUD, P. & BRUMMELL, N. 2015 2D or not 2D: the effect of dimensionality on the dynamics of fingering convection at low Prandtl number. *Astrophys. J.* **815**, 42.
- GOLUSKIN, D., JOHNSTON, H., FLIERL, G. R. & SPIEGEL, E. A. 2014 Convectively driven shear and decreased heat flux. *J. Fluid Mech.* **759**, 360–385.
- GOUGH, D. O., SPIEGEL, E. A. & TOOMRE, J. 1975 Modal equations for cellular convection. *J. Fluid Mech.* **68**, 695–719.
- GOUGH, D. O. & TOOMRE, J. 1982 Single-mode theory of diffusive layers in thermohaline convection. *J. Fluid Mech.* **125**, 75–97.
- GRAHAM, M. D. & FLORYAN, D. 2021 Exact coherent states and the nonlinear dynamics of wall-bounded turbulent flows. *Annu. Rev. Fluid Mech.* **53**, 227–253.
- HAGE, E. & TILGNER, A. 2010 High Rayleigh number convection with double diffusive fingers. *Phys. Fluids* **22**, 076603.
- HERRING, J. R. 1963 Investigation of problems in thermal convection. *J. Atmos. Sci.* **20**, 325–338.
- HERRING, J. R. 1964 Investigation of problems in thermal convection: rigid boundaries. *J. Atmos. Sci.* **21**, 277–290.
- HOLYER, J. Y. 1981 On the collective instability of salt fingers. *J. Fluid Mech.* **110**, 195–207.
- HOLYER, J. Y. 1984 The stability of long, steady, two-dimensional salt fingers. *J. Fluid Mech.* **147**, 169–185.
- HOWARD, L. N. & KRISHNAMURTI, R. 1986 Large-scale flow in turbulent convection: a mathematical model. *J. Fluid Mech.* **170**, 385–410.
- JULIEN, K. & KNOBLOCH, E. 1997 Fully nonlinear oscillatory convection in a rotating layer. *Phys. Fluids* **9**, 1906–1913.
- JULIEN, K. & KNOBLOCH, E. 2007 Reduced models for fluid flows with strong constraints. *J. Math. Phys.* **48**, 065405.
- JULIEN, K., KNOBLOCH, E. & TOBIAS, S. 1999 Strongly nonlinear magnetoconvection in three dimensions. *Physica D* **128**, 105–129.
- JULIEN, K., KNOBLOCH, E. & TOBIAS, S. M. 2000 Nonlinear magnetoconvection in the presence of strong oblique fields. *J. Fluid Mech.* **410**, 285–322.
- KAWAHARA, G. & KIDA, S. 2001 Periodic motion embedded in plane Couette turbulence: regeneration cycle and burst. *J. Fluid Mech.* **449**, 291–300.
- KAWAHARA, G., UHLMANN, M. & VAN VEEN, L. 2012 The significance of simple invariant solutions in turbulent flows. *Annu. Rev. Fluid Mech.* **44**, 203–225.
- KNOBLOCH, E., DEANE, A. E., TOOMRE, J. & MOORE, D. R. 1986 Doubly diffusive waves. *Contemp. Math.* **56**, 203–216.
- KNOBLOCH, E., PROCTOR, M. R. E. & WEISS, N. O. 1992 Heteroclinic bifurcations in a simple model of double-diffusive convection. *J. Fluid Mech.* **239**, 273–292.
- KRISHNAMURTI, R. 2003 Double-diffusive transport in laboratory thermohaline staircases. *J. Fluid Mech.* **483**, 287–314.
- KRISHNAMURTI, R. 2009 Heat, salt and momentum transport in a laboratory thermohaline staircase. *J. Fluid Mech.* **638**, 491–506.

- KRISHNAMURTI, R. & HOWARD, L. N. 1981 Large-scale flow generation in turbulent convection. *Proc. Natl. Acad. Sci.* **78** (4), 1981–1985.
- LEWIS, S., REES, D. A. S. & BASSOM, A. P. 1997 High wavenumber convection in tall porous containers heated from below. *Q. J. Mech. Appl. Math.* **50**, 545–563.
- LI, J. & YANG, Y. 2022 On the wall-bounded model of fingering double diffusive convection. *arXiv preprint* p. arXiv:2204.03142.
- LINDEN, P. F. 1978 The formation of banded salt finger structure. *J. Geophys. Res.: Oceans* **83** (C6), 2902–2912.
- LOPEZ, J. M. & MURPHY, J. O. 1983 Time-dependent thermal convection. *Publ. Astron. Soc. Aust.* **5**, 173–175.
- LUCAS, D., CAULFIELD, C. P. & KERSWELL, R. R. 2017 Layer formation in horizontally forced stratified turbulence: connecting exact coherent structures to linear instabilities. *J. Fluid Mech.* **832**, 409–437.
- LUCAS, D., CAULFIELD, C. P. & KERSWELL, R. R. 2019 Layer formation and relaminarisation in plane Couette flow with spanwise stratification. *J. Fluid Mech.* **868**, 97–118.
- MALKUS, W. V. R. & VERONIS, G. 1958 Finite amplitude cellular convection. *J. Fluid Mech.* **4**, 225–260.
- MASSAGUER, J. M. & MERCADER, I. 1988 Instability of swirl in low-Prandtl-number thermal convection. *J. Fluid Mech.* **189**, 367–395.
- MASSAGUER, J. M., MERCADER, I. & NET, M. 1990 Nonlinear dynamics of vertical vorticity in low-Prandtl-number thermal convection. *J. Fluid Mech.* **214**, 579–597.
- MATTHEWS, P. C., PROCTOR, M. R. E., RUCKLIDGE, A. M. & WEISS, N. O. 1993 Pulsating waves in nonlinear magnetoconvection. *Phys. Lett. A* **183**, 69–75.
- MORELL, J. M., CORREDOR, J. E. & MERRYFIELD, W. J. 2006 Thermohaline staircases in a Caribbean eddy and mechanisms for staircase formation. *Deep Sea Res. Part II* **53**, 128–139.
- MUENCH, R. D., FERNANDO, H. J. S. & STEGEN, G. R. 1990 Temperature and salinity staircases in the northwestern Weddell Sea. *J. Phys. Oceanogr.* **20**, 295–306.
- MURPHY, J. O. & LOPEZ, J. M. 1984 The influence of vertical vorticity on thermal convection. *Aust. J. Phys.* **37**, 179–196.
- OGLETHORPE, R. L. F., CAULFIELD, C. P. & WOODS, A. W. 2013 Spontaneous layering in stratified turbulent Taylor-Couette flow. *J. Fluid Mech.* **721**, R3.
- PADMAN, L. & DILLON, T. M. 1989 Thermal microstructure and internal waves in the Canada Basin diffusive staircase. *Deep Sea Res. Part A* **36**, 531–542.
- PAPARELLA, F. 1997 A few steps toward staircases. *Double-Diffusive Processes, 1996 Summer Study Program in Geophysical Fluid Dynamics* pp. 232–247.
- PAPARELLA, F. & SPIEGEL, E. A. 1999 Sheared salt fingers: Instability in a truncated system. *Phys. Fluids* **11**, 1161–1168.
- PAPARELLA, F., SPIEGEL, E. A. & TALON, S. 2002 Shear and mixing in oscillatory doubly diffusive convection. *Geophys. Astrophys. Fluid Dyn.* **96**, 271–289.
- PHILLIPS, O. M. 1972 Turbulence in a strongly stratified fluid—Is it unstable? In *Deep Sea Res. Oceanogr. Abstr.*, , vol. 19, pp. 79–81. Elsevier.
- PIACSEK, S. A. & TOOMRE, J. 1980 Nonlinear evolution and structure of salt fingers. *Marine Turbulence, Proceedings of The 11th International Liège Colloquium on Ocean Hydrodynamics* **28**, 193–219.
- PLUMLEY, M., CALKINS, M. A., JULIEN, K. & TOBIAS, S. M. 2018 Self-consistent single mode investigations of the quasi-geostrophic convection-driven dynamo model. *J. Plasma Phys.* **84**, 735840406.
- VAN DER POEL, E. P., STEVENS, R. J. A. M. & LOHSE, D. 2013 Comparison between two-and three-dimensional Rayleigh–Bénard convection. *J. Fluid Mech.* **736**, 177–194.
- POSMENTIER, E. S. 1977 The generation of salinity finestructure by vertical diffusion. *J. Phys. Oceanogr.* **7**, 298–300.
- PROCTOR, M. R. E. & HOLYER, J. Y. 1986 Planform selection in salt fingers. *J. Fluid Mech.* **168**, 241–253.
- PROCTOR, M. R. E. & WEISS, N. O. 1993 Symmetries of time-dependent magnetoconvection. *Geophys. Astrophys. Fluid Dyn.* **70**, 137–160.
- PROCTOR, M. R. E., WEISS, N. O., BROWNJOHN, D. P. & HURLBURT, N. E. 1994 Nonlinear compressible magnetoconvection Part 2. Streaming instabilities in two dimensions. *J. Fluid Mech.* **280**, 227–253.
- RADEMACHER, J. D. M. & UECKER, H. 2017 Symmetries, freezing, and Hopf bifurcations of traveling waves in pde2path. <https://www.staff.uni-oldenburg.de/hannes.uecker/pde2path/>.
- RADKO, T. 2003 A mechanism for layer formation in a double-diffusive fluid. *J. Fluid Mech.* **497**, 365–380.
- RADKO, T. 2005 What determines the thickness of layers in a thermohaline staircase? *J. Fluid Mech.* **523**, 79–98.

- RADKO, T. 2010 Equilibration of weakly nonlinear salt fingers. *J. Fluid Mech.* **645**, 121–143.
- RADKO, T. 2013 *Double-diffusive Convection*. Cambridge University Press.
- RADKO, T. 2016 Thermohaline layering in dynamically and diffusively stable shear flows. *J. Fluid Mech.* **805**, 147–170.
- RADKO, T. & STERN, M. E. 1999 Salt fingers in three dimensions. *J. Mar. Res.* **57**, 471–502.
- RADKO, T. & STERN, M. E. 2000 Finite-amplitude salt fingers in a vertically bounded layer. *J. Fluid Mech.* **425**, 133–160.
- RHINES, P. B. & YOUNG, W. R. 1983 How rapidly is a passive scalar mixed within closed streamlines? *J. Fluid Mech.* **133**, 133–145.
- RUCKLIDGE, A. M. & MATTHEWS, P. C. 1996 Analysis of the shearing instability in nonlinear convection and magnetoconvection. *Nonlinearity* **9**, 311–351.
- SCHMID, P. J. & HENNINGSON, D. S. 2012 *Stability and Transition in Shear Flows*. Springer Science & Business Media.
- SCHMITT, R. W., LEDWELL, J. R., MONTGOMERY, E. T., POLZIN, K. L. & TOOLE, J. M. 2005 Enhanced diapycnal mixing by salt fingers in the thermocline of the tropical Atlantic. *Science* **308** (5722), 685–688.
- SCHMITT, R. W., PERKINS, H., BOYD, J. D. & STALCUP, M. C. 1987 C-SALT: An investigation of the thermohaline staircase in the western tropical North Atlantic. *Deep Sea Res. Part A* **34**, 1655–1665.
- SIGGIA, E. D. 1994 High Rayleigh number convection. *Annu. Rev. Fluid Mech.* **26**, 137–168.
- SPEAR, D. J. & THOMSON, R. E. 2012 Thermohaline staircases in a British Columbia fjord. *Atmos. Ocean* **50**, 127–133.
- ST. LAURENT, L. & SCHMITT, R. W. 1999 The contribution of salt fingers to vertical mixing in the North Atlantic Tracer Release Experiment. *J. Phys. Oceanogr.* **29**, 1404–1424.
- STELLMACH, S., TRAXLER, A., GARAUD, P., BRUMMELL, N. & RADKO, T. 2011 Dynamics of fingering convection. Part 2 The formation of thermohaline staircases. *J. Fluid Mech.* **677**, 554–571.
- STERN, M. E. 1969 Collective instability of salt fingers. *J. Fluid Mech.* **35**, 209–218.
- TAIT, R. I. & HOWE, M. R. 1968 Some observations of thermo-haline stratification in the deep ocean. *Deep Sea Res. Oceanogr. Abstr.* **15**, 275–280.
- TAIT, R. I. & HOWE, M. R. 1971 Thermohaline staircase. *Nature* **231** (5299), 178–179.
- TAYLOR, J. & BUCENS, P. 1989 Laboratory experiments on the structure of salt fingers. *Deep Sea Res. Part A* **36**, 1675–1704.
- TAYLOR, J. R. & ZHOU, Q. 2017 A multi-parameter criterion for layer formation in a stratified shear flow using sorted buoyancy coordinates. *J. Fluid Mech.* **823**, R5.
- TIMMERMAN, M.-L., TOOLE, J., KRISHFIELD, R. & WINSOR, P. 2008 Ice-Tethered Profiler observations of the double-diffusive staircase in the Canada Basin thermocline. *J. Geophys. Res. Oceans* **113**, C00A02.
- TOOMRE, J., GOUGH, D. O. & SPIEGEL, E. A. 1977 Numerical solutions of single-mode convection equations. *J. Fluid Mech.* **79**, 1–31.
- UECKER, H. 2021a *Numerical Continuation and Bifurcation in Nonlinear PDEs*. SIAM.
- UECKER, H. 2021b pde2path without finite elements. <https://www.staff.uni-oldenburg.de/hannes.uecker/pde2path/>.
- UECKER, H., WETZEL, D. & RADEMACHER, J. D. M. 2014 pde2path: A Matlab package for continuation and bifurcation in 2D elliptic systems. *Numer. Math. Theory Methods Appl.* **7**, 58–106.
- VAN VEEN, L., KIDA, S. & KAWAHARA, G. 2006 Periodic motion representing isotropic turbulence. *Fluid Dyn. Res.* **38**, 19–46.
- WANG, Q., VERZICCO, R., LOHSE, D. & SHISHKINA, O. 2020 Multiple states in turbulent large-aspect-ratio thermal convection: What determines the number of convection rolls? *Phys. Rev. Lett.* **125**, 074501.
- WEIDEMAN, J. A. & REDDY, S. C. 2000 A MATLAB differentiation matrix suite. *ACM Trans. Math. Software* **26**, 465–519.
- XIA, Z., SHI, Y., CAI, Q., WAN, M. & CHEN, S. 2018 Multiple states in turbulent plane Couette flow with spanwise rotation. *J. Fluid Mech.* **837**, 477–490.
- XIE, J.-H., JULIEN, K. & KNOBLOCH, E. 2019 Jet formation in salt-finger convection: a modified Rayleigh–Bénard problem. *J. Fluid Mech.* **858**, 228–263.
- XIE, J.-H., MIQUEL, B., JULIEN, K. & KNOBLOCH, E. 2017 A reduced model for salt-finger convection in the small diffusivity ratio limit. *Fluids* **2** (1), 6.
- YANG, X. & XIA, Z.-H. 2021 Bifurcation and multiple states in plane Couette flow with spanwise rotation. *J. Fluid Mech.* **913**, A49.

- YANG, Y., CHEN, W., VERZICCO, R. & LOHSE, D. 2020 Multiple states and transport properties of double-diffusive convection turbulence. *Proc. Natl. Acad. Sci.* **117** (26), 14676–14681.
- YANG, Y., VAN DER POEL, E. P., OSTILLA-MÓNICO, R., SUN, C., VERZICCO, R., GROSSMANN, S. & LOHSE, D. 2015 Salinity transfer in bounded double diffusive convection. *J. Fluid Mech.* **768**, 476–491.
- YANG, Y., VERZICCO, R. & LOHSE, D. 2016a Scaling laws and flow structures of double diffusive convection in the finger regime. *J. Fluid Mech.* **802**, 667–689.
- YANG, Y., VERZICCO, R. & LOHSE, D. 2016b Vertically bounded double diffusive convection in the finger regime: Comparing no-slip versus free-slip boundary conditions. *Phys. Rev. Lett.* **117**, 184501.
- YANG, Y., VERZICCO, R., LOHSE, D. & CAULFIELD, C. P. 2022 Layering and vertical transport in sheared double-diffusive convection in the diffusive regime. *J. Fluid Mech.* **933**, A30.
- ZAHN, J.-P., TOOMRE, J., SPIEGEL, E. A. & GOUGH, D. O. 1974 Nonlinear cellular motions in Poiseuille channel flow. *J. Fluid Mech.* **64**, 319–346.
- ZHANG, X., WANG, L.-L., LIN, C., ZHU, H. & ZENG, C. 2018 Numerical study on tilting salt finger in a laminar shear flow. *Phys. Fluids* **30**, 022110.
- ZODIATIS, G. & GASPARINI, G. P. 1996 Thermohaline staircase formations in the Tyrrhenian Sea. *Deep Sea Res. Part I* **43**, 655–678.